ABSTRACT

Title of Thesis: Using Shear Waves to Characterize a Firn Aquifer on the Helheim Glacier in Southeast Greenland

Jonathan Guandique, Master of Science, 2019

Thesis Directed By: Professor Nicholas Schmerr
Department of Geology

The Greenland ice sheet is melting at an accelerating rate due to increasing global average temperatures. Ice penetrating radar surveys and ice cores extracted from the southeastern margin of the Greenland ice sheet near Helheim glacier discovered that a liquid water aquifer has formed within the near surface recrystallized and compacted snow (firn). Here we use active source seismology to probe the structure of this aquifer in the firn, and present results from a joint inversion technique that uses S-waves, P-waves, and surface waves to constrain the attenuation and seismic velocities that inform on the liquid water stored within the aquifer. Confirming past studies, we find that the aquifer lies at 27.9 ± 3.5 m and has an approximate thickness of 10 ± 4 m. We determine there is 1565 ± 769 kg m^{-2} of water within the aquifer, a downward revision from past studies. Our study of S-waves and surface waves identified a complex structure in the aquifer layer and future work must incorporate full waveform modeling to use these waves for understanding firn aquifers.

USING SHEAR WAVES TO CHARACTERIZE A FIRN AQUIFER ON THE HELHEIM GLACIER IN SOUTHEAST GREENLAND

by

Jonathan Guandique

Thesis submitted to the Faculty of the Graduate School of the
University of Maryland, College Park, in partial fulfillment
of the requirements for the degree of
Master of Science
2019

Advisory Committee:
Professor Nicholas Schmerr, Chair
Professor Mong-Han Huang
Professor Karen Prestegaard

© Copyright by
Jonathan Guandique
2019

Acknowledgements

I would like to show my appreciation to all that have provided me with the support that made my graduate experience possible.

I would first like to thank my advisor, Dr. Nicholas Schmerr, for the opportunity to work on this project and learn and grow as a scientist over the past two years. When I felt like I had reached an impasse, or felt as though I was not doing enough, he would reassure me of my hard work and always provide constructive, yet positive and uplifting, feedback. It has been a pleasure to work with such a great scholar.

I would like to thank my committee, Dr. Mong-Han Huang and Dr. Karen Prestegaard, for serving on the thesis committee for taking time out of their busy schedules to review the manuscript.

I would like to thank Scott Burdick, whose code was used in this project and Chao Gao, who specialized the code to fit my project. I would like to thank Dr. Ross Maguire for his help in the modeling process. Whenever I had any questions on coding, they would never hesitate to help and always make themselves available.

I would like to thank my colleagues in the seismology lab, as well as my colleagues in the department who have made my graduate school experience an enjoyable one.

Lastly, I would like to thank my friends and family that have supported me physically and emotionally. I do not have enough words to express my gratitude to them. Thank you all for your support.

Table of Contents

Acknowledgements ii
Table of Contents iii
List of Figures iv
List of Abbreviations v
Chapter 1: Introduction 1
1.1: Background 1
1.2: Applications of Active Source Seismology to Ice/Firn 6
1.3: Active Source Seismology on the Helheim Glacier 10
Chapter 2: Methods 13
2.1: Data Processing 13
2.2: Data Inversion 16
Chapter 3: Results 20
3.1: Joint Inversions 20
3.1.1: Joint Inversion 1- P-waves and Surface waves 22
3.1.2: Joint Inversion 2- P-Waves and S-waves 25
3.1.3: Joint Inversion 3- P-waves, S-waves, and Surface waves 28
3.2: Calculating Water Content and Volume 32
Chapter 4: Discussion and Conclusion 36
4.1: Implications of a Low Velocity Zone 37
4.1.1: Synthetic Modeling 40
4.1.2: Synthetic Seismograms 42
4.2: Reliability of Joint Inversions 45
4.3: Water content across Greenland 53
4.4: Future Work 55
4.5: Conclusions 57
Appendices 60
Bibliography 80

List of Figures

Figure 1.1……10

Figure 1.2……11

Figure 2.1……16

Figure 2.2……19

Figure 2.3……19

Figure 3.1……24

Figure 3.2……27

Figure 3.3……30

Figure 3.4……31

Figure 3.5……31

Figure 3.6……34

Figure 3.7……35

Figure 4.1……38

Figure 4.2……39

Figure 4.3……41

Figure 4.4……44

Figure 4.5……49

Figure 4.6……51

List of Abbreviations

GIS = Greenland Ice Sheet

GPR = Ground penetrating radar

Gt =gigatons

L1 = Layer 1

L2 = Layer 2

L3 = Layer 3

LWC = Liquid Water content

LVZ = Low velocity zone

rj-McMC = Reversible jump Markov chain Monte Carlo

V_P = Velocity of the P-waves

V_S = Velocity of the S-waves

Chapter 1: Introduction

1.1: Background

The worldwide decline of glaciers and sustained degradation of the cryosphere are direct consequences of global climate change. Increasing global temperature averages have caused parts of the Greenland Ice sheet (GIS) to melt at an alarming rate, exceeding 535 Gt/a (*Enderlin et al. 2014*). Although the mass budget is variable from year to year, an observable increase total mass loss of the GIS has been observed and attributed to increased surface melting, runoff, and ice discharge from marine-terminating glaciers (*Enderlin et al*. 2014, *Rignot et al.* 2011). In Greenland, ice dynamics via ice discharge accounts for two-thirds of its mass loss, and the rest of the mass loss from increased runoff and decreased accumulation (Rignot *et al.* 2006). Diurnal and seasonal variations imply a steady state between the freezing and melting processes in the ice sheet (McGrath *et al.* 2011), where accumulation of snow and the freezing of surface melt is expected during the winter, while ablation and melting of snow occurs during the summer. The ablation zone is predominantly glacial ice, while snow and firn dominate the accumulation zone, firn being the transitional material from snow to glacial ice (Fountain *et al.* 1998). Although some regions of the GIS have not shown mass loss since 1960, present-day mass loss persists in the warming climate setting near ice sheet margins (Rignot *et al*. 2011). Past studies have assumed surface melt to simply discharge into the ocean (Drinkwater *et al.* 2001; Fettweis *et*

al. 2011). However, there is new evidence for the accumulation and perhaps storage of liquid water in sub- and supra-glacial environments of the Greenland ice sheet.

A new type of melt feature, the perennial storage of liquid water in the firn of southeastern Greenland, has been detected by radar surveys over the last decade (*Chu et al.* 2018; *Forster et al.* 2014; *Miège et al.* 2016; *Rignot et al.* 2012). These firn aquifers extend to a depth of 25-30 m and span an area of 17,920 km^2 - 21,900 km^2 in the vicinity of the Helheim glacier (*Miège et al.* 2016; *Montgomery et al.* 2017). Firn aquifers originate from the accumulation of surface melt drainage in the percolation zone of the firn, concentrating liquid above the solid ice layer (*Forster et al.* 2014; *Munneke et al.* 2014, *Zwally et al.* 2002). When refreezing occurs in the winter, the ice releases latent heat during the phase change process, which is absorbed by the surrounding water and keeping the aquifer liquid during the winter (*Steger et al.* 2017). Furthermore, an insulating effect is generated by the 300 – 360 mm/yr of fresh snowfall during the winter, allowing subsurface water to remain liquid (*Forster et al.* 2014; *Hakuba et al.* 2012; *Steger et al.* 2017). The underlying hydrology and flux of the liquid water from the firn aquifers into the englacial system is unknown, and the focus of our study.

Annually, firn is created through deposition and compaction of snow. As more snow is accumulated, it compresses the underlying snow. This drives recrystallization, and increases ice grain size, reducing the amount of pore space in the zone through which liquid water can percolate. The base of the firn aquifer is thus correlated to a depth where compaction closes the continuous pore space, i.e., a pore closure depth and loss of permeability through the ice (*Koenig et al.* 2014;

Montgomery et al. 2017). This depth is defined by the solidus temperature and pressure for the liquid phase, as any liquid water saturating the pore space that freezes will close porosity (*Lliboutry et al.* 1996). Aquifers are thus stable to a limited depth and continued accumulation of melt will eventually saturate the entirety of the firn column, resulting in surficial lakes if water cannot enter the subglacial system.

The evolution of this system is dependent upon the availability of liquid water produced through melt at the surface, and lateral transport within the system. Throughout the melt season, surface water drains into the percolation zone and forms a complex subglacial hydrological system that transports meltwater. If there is significant drainage, the warmer waters would expand preexisting pores in the firn through melting, enabling further drainage of surface water into the system (*McGrath et al.* 2011). Surface melt drainage creates "pipes" or pathways that the surface water travel through as it is melting the surrounding ice, further enhancing flow into the system (*Pfeffer and Humphrey* 1996). During the winter season, these pipes refreeze, and near surface pore spaces containing meltwater refreeze into ice lenses, creating a complex, heterogenous ice stratigraphy in which the surface melt water must traverse (*Miège et al*. 2016; *Miller et al.* 2017; *Pfeffer and Humphrey* 1996, *Vaňková et al.* 2018). Thus, the amount of water that can be accommodated in the firn aquifer is controlled by the amount of water draining into the glacier, as well as the evolving porosity at depth (*Miller et al.* 2017; *Pfeffer and Humphrey* 1996).

To quantify the water abundance and porosity structure of firn aquifer systems, these properties have been investigated using seismic data and Ground Penetrating Radar (GPR) to determine the depth to the snow/ice transition (*Godio and*

Rege 2015), and to map water deep underneath glaciers (*Christianson et al.* 2012; *Horgan et al.* 2012). Recent discoveries of perennial aquifers, surface lakes and their contribution to water drainage, raise questions about the communication and pathways of this liquid water into the deep glacial system. There is evidence to suggest that the drainage of surface melt from glacial lakes and firn aquifers can increase the velocities of ice flow, either by creating new cracks or destabilizing existing ones within the glacier early in the melting season bringing liquid to the bed (*Chandler et al. 2013*; *Hoffman et al. 2011*; *Palmer et al. 2011*). This indicates that glacial dynamics may be influenced by the meltwater process within the glacier beyond the consideration of the volume of surface melt alone (*Flowers* 2018).

This brief review of the importance of firn aquifers indicates that determining the volume of water in these aquifers is essential to the understanding of glacier dynamics. Geophysical methods provide the best opportunity to evaluate firn aquifer thickness and lateral extent that inform on these properties. Radar surveys provide a large areal data coverage and are an ideal tool for detecting the presence and depth of the water table. However, radar energy does not readily penetrate the liquid water, making it difficult to estimate the thickness of the saturated zone. Ground-penetrating radar surveys on glaciers have primarily been used to determine subglacial hydrological processes at depths of 100s of meters. The instruments used in these surveys usually have a source that emit low bandwidths, ranging from 10-80 MHz (Ross *et al.* 2018). Instruments used for shallow surface surveys emit higher bandwidths (> 200 MHz or a resolution depth of 1s-10s of meters), but do not penetrate as deeply into the ice sheet. The resolution of these types of radars are

generally a function of bandwidth and center frequency; as frequency is increased, the finer the resolution, but the penetration depth of the signal is decreased (e.g. 0.5 m resolution at 200 MHz) (Moorman *et al.* 2000).

Similar to radar surveys, airborne radar surveys detect the areal extent of the aquifers. For example, airborne radio echo soundings, such as the one used by Jordan et al. (2018), penetrate the upper 20 m to detect a wet-dry transition in the glacier. While airborne radar surveys can collect data across a large area, the speed of the moving aircraft conducting these surveys can result in poor resolution in depth and extent. The high frequency emitted from airborne surveys are insensitive to thin ice margins. Thus, airborne surveys are not ideal for accurate and detailed ice-aquifer thickness measurements but are useful in detecting the presence of an aquifer system in a larger and more general scale. (*Ross et al.* 2017).

In-situ geophysical techniques that are sensitive to shallow water include active-source seismology and magnetic-resonance sounding. Both techniques can provide high spatial resolution of the water table. Magnetic resonance sounding (MRS) method (*Legchenko et al.* 2018) transmits a low frequency electromagnetic field that excites the hydrogen molecules within the medium below, and the resulting resonance frequency emitted by the water hydrogen atoms is proportional to the abundance of liquid water present. The accuracy of the water volume is dependent on the forward modeling and subsequent inversions and calibration of the MRS signal. The results are non-unique and dependent upon choices for thickness of the aquifer, even in a relatively homogeneous subsurface such as that of Greenland (*Legchenk*o *et al.* 2018). MRS resolution of the layer is dependent on its thickness and depth, the

deeper and thicker a layer is, the more resolvable it is, and vice versa (*Legchenko et al.* 2018). MRS and radar combined (*Legchenko et al.* 2018) can improve estimates of water content, but are limited without any constraint on aquifer thickness, which must either be measured directly from ice cores or inferred by high frequency seismology. Thus, a combination of techniques is needed to best elucidate water content. Here we focus on how a high frequency active source seismology investigation can provide improved estimates for aquifer water content and thickness that will ultimately feed into these other geophysical methods.

1.2: Applications of Active Source Seismology to Ice/Firn

Active source seismology uses artificial sources of seismic energy (e.g. hammers, explosives) recorded at an array of seismic stations with precisely known locations. These surveys provide a relatively inexpensive method of imaging the shallow subsurface in a smalltime window and at high frequencies (>50 Hz). Seismic sources generate seismic energy, in the form of compressional waves (P-waves) and shear waves (S-waves and surface waves). These waves travel downward at an angle of incidence (angle between the horizontal surface and the path the energy is traveling) through layers and refract where there are changes in velocity of the underlying media (*Aki and Richards* 1980). Any differences in the velocity structure can be estimated by measuring the travel time curves (i.e. travel times as a function of distance between the source and receiver) of the P- and S-waves. Changes in the slope of the refracted waves are indicative of velocity changes with depth.

The velocity of the P-wave, given by Equation (1), is sensitive to the bulk modulus κ (Gpa), shear modulus μ (GPa), and density ρ (kg m^{-3}) of a material, and

are the result of dilation or volume change in the elastic media: (*Aki and Richards* 1980)

$$V_P = \sqrt{\frac{\kappa + \frac{4}{3}\mu}{\rho}} \qquad (1)$$

The S-wave velocity, given by Equation (2), is sensitive to the shear modulus μ and density (*Aki and Richards* 1980), and are the results of shearing a solid.

$$V_S = \sqrt{\frac{\mu}{\rho}} \qquad (2)$$

The bulk modulus is the incompressibility, or resistance to compression, of a material. In firn, the bulk modulus typically increases as pore space decreases from compression. Similar to κ, the shear modulus μ is the rigidity of a material. The shear modulus in firn increases as firn is compacted. However, the presence of liquid water reduces the shear modulus to zero, as there is no rigidity to water, a fluid. The density ρ is controlled by the state of the ice or water in the subsurface (Figure 1.1). The firn has a low density due to being highly porous, air-filled, and mostly unconsolidated. The saturated firn has a higher density, due to the replacement of pore space air by water and the increase in the amount of ice. The solid ice lacks is less dense than the saturated firn owing to the decrease in density of water as it goes from liquid to solid, but is more dense than unsaturated firn (Table 1).

S-waves are slower than P-waves, exhibit no volume change, and cannot travel through liquids (*Aki and Richards* 1980, *Stein and Wysession 2003*). An

increase in the fraction of liquid subsurface will reduce the velocity of S-waves. However, in the firn, the pore space is filled with air, also a fluid. In Greenland, since the firn aquifer is not completely liquid, rather, it is an ice layer saturated with water and higher density, so an observable decrease in the velocities of the S-waves could be detected. Lower density in the unsaturated firn is due to larger and poorly consolidated grains of firn with air-filled pores. The presence of water in the firn increases the density of the system consolidation of the ice grains. The shear modulus is controlled by the continuity of the individual firn grains and presence of ice layers.

Table 1*: Density and Velocities of firn and ice*

Parameter	Value	Source
V_{Psnow} (m s^{-1})	500-1000	*Johnson (1981), Sommerfield (1982)*
V_{Pfirn} (m s^{-1})	1000-2200	*Clarke and Echelmeyer (1996), Godio and Rege (2015)*
V_{Pice} (m s^{-1})	3400-3800	*Kirchner and Bently (1979), Godio and Rege (2015), Montgomery et al. (2017)*
V_{PH2O} (m s^{-1})	1450	*Shearer (2009)*
V_{Sfirn} (m s^{-1})	600-1400	*Armstrong (2009)*
V_{Sice} (m s^{-1})	1500-1800	*Kirchner and Bentley (1979), Godio and Rege (2015)*
ρ_{snow} (kg m^{-3})	300 – 330	*Munneke et al. (2014), Armstrong (2009)*
ρ_{firn} (kg m^{-3})	Dry: 490-600 Wet: 650-780	*Kawashima et al. (1993), Huss (2013), Munneke et al. (2014), Miller et al. (2017)*
ρ_{H2O} (kg m^{-3})	1000	*Shearer (2009)*

ρ_{ice} (kg/m^3)	815 - 920	*Shumskiy (1960), Huss (2013), Godio and Rege (2015), Miller et al. (2018)*

A parameter sensitive to fluid content is the V_P/V_S ratio. We can take the V_P/V_S ratio to better identify presence of liquid water since V_P/V_S may be more sensitive to the liquid than V_P or V_S may be individually (*Hamada* 2004). The V_P/V_S ratio has been used to identify the presence of fluids at depth (*Biot* 1962, *Lee* 2003) and may serve as a constraint in determining the water content and layering within the firn aquifer system.

In addition to direct P- and S-waves, use of surface waves that are generated by active source experiments can constrain aquifer structure. Surface waves are seismic waves that propagate along the surface and are sensitive to shallow structure and low-frequency source properties (*Shearer* 2009). The surface waves are dispersive where velocity increases with depth. Surface waves are either horizontally (Love waves) or vertically (Rayleigh waves) polarized (*Stein and Wysession* 2003). Surface wave phase velocity is frequency dependent because waves of different frequency are sensitive to different depth ranges. High frequency surface waves travel with shorter wavelengths and are thus more sensitive to shallow structure than their lower frequency counterparts (*Shearer* 2009). Longer wavelengths typically exhibit greater phase velocities as they penetrate deeper into the subsurface and are more sensitive to the elastic properties if higher velocity layers are found at depth (*Xia et al.* 1999). As a result, surface waves tend to exhibit characteristic dispersion. Since a given wavelength is accompanied with a unique frequency, the dispersion curve of the seismic signal can be found by measuring the move out of a surface wave phase

train across narrowly banded filters. The resulting phase velocity dispersion curve is used as another constraint in an inversion for P- and S- wave velocity as a function of depth.

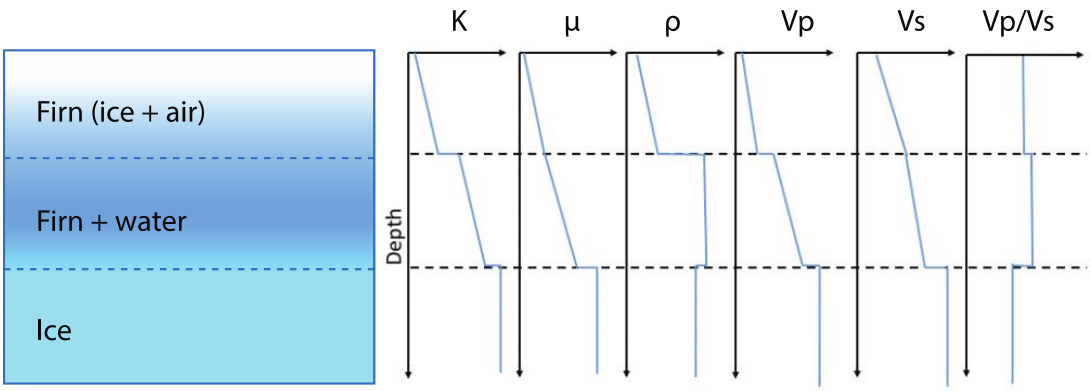

Figure 1.1: Simple 3-layer interpretation of the firn aquifer system. Hypothetical seismic scenario for a firn aquifer system, using the properties of firn, ice, water, and air presented in Table 1. Compaction is assumed to reduce pore space with depth increasing the κ and μ, while density is controlled by the relative proportions of ice, air and water. We assume the firn layer is saturated in water.

1.3: Active Source Seismology on the Helheim Glacier

To determine the aquifer depth, an active-source refraction seismic survey was conducted in 2015 and 2016 along the Helheim glacier in southeast Greenland to temporally and spatially sample the structure of firn aquifer. Previous analysis of the data from this survey by Montgomery et al. (2017) reported the aquifer at a depth of 27.7 ± 2.9 m under the surface, with an average thickness of 11.5 ± 5.5 m.

The active-source seismology profile was conducted over a profile of 15 km, with the experiments spaced every 1-2 km (Fig. 1.2). This line followed the local ice flow velocity of the Helheim Glacier. The instruments were 40 Hz vertical component geophones spaced every 5 m, and data were recorded by a Geometrics Geode multi-channel data recorder, using a record length of 1 s and a sampling rate of 16 kHz, or 62.5 μs per sample (*Montgomery et al.* 2017). The active seismic source

for the experiment was generated by an 8-kg sledgehammer striking a 30x30x1.5 cm thick steel plate (Montgomery *et al.* 2017). Two different array geometries were used in 2015 and 2016, such that the 2015 array geometry yielded a sampling depth of ~30 m, while the 2016 array geometry yields a sampling depth of ~50 m (Fig 1.2). The geophones were buried ~10 cm below the surface to minimize the effects of sources of noise such as wind, distant anthropogenic generator noise, small firn disturbances, and human movement. Multiple hammer strikes (or shots) were stacked to maximize the signal to noise ratio (Montgomery et al. 2017).

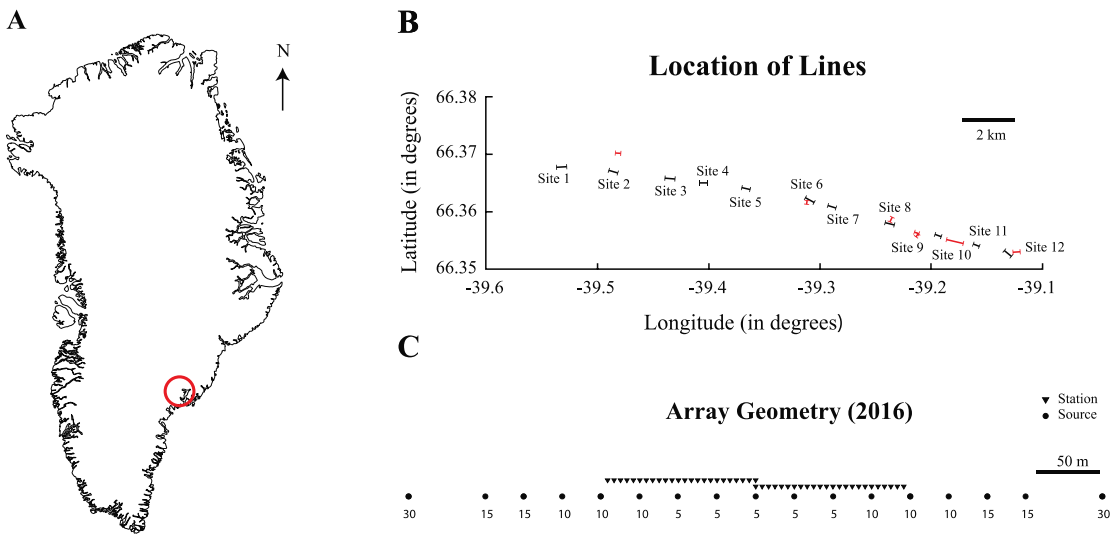

Figure 1.2: Location of field site and array geometry for the seismic experiment conducted in southeastern Greenland. A) Geographic location of the field site on the Helheim Glacier (red circle). **B)** Location of the seismic refraction experiments conducted by Montgomery *et al.* (2017). Data from 2015 in red, data from 2016 in black. **C)** Geometry of the geophones and hammer strikes for the data set collected in 2016.

Here, we build on the P-wave velocity and water content analysis conducted by Montgomery et al. (2017) and incorporate information from S-waves, surface waves, and attenuation, as joint constraints for an inversion for the water stored of the aquifer. We construct a joint model of P- and S- wave velocity to test for the

sensitivity of the liquid by examining the travel times and amplitudes of P-waves, S-waves and surface wave dispersion in the field data. This additional data should better constrain the dimensions of the aquifer and incorporate additional information contained in the S-wave and surface wave velocities.

There is a tradeoff in the P-wave analysis due to the presence of air bubbles in the saturated firn (*Virieux* 1986). Theoretically, shear waves are insensitive to the relative air/water fraction in the pores and only are sensitive to the total pore space. Using a porosity derived by the shear waves provides a true porosity measurement and comparing it to a porosity derived from the P-waves is indicative of the water content found within the saturated firn Shear waves traveling through the saturated firn aquifer are theoretically more sensitive to the underlying transition from water to ice (Fig 1.1) and are predicted to have a stronger reflection coefficient at the firn/ice transition than the P-waves. The Rayleigh surface wave data should be sensitive to P- and S- waves and provide information on both the top and bottom of the aquifer as well as the amount of liquid water content (LWC). The goal of our study is to combine this information and learn more about the liquid water present within the Helheim aquifer system and firn across the Greenland ice sheet in general.

Chapter 2: Methods

2.1: Data Processing

Our dataset consists of the seismic traces generated by active source seismic experiment, presented as an assembled dataset from IRIS (Incorporated Research Institutions for Seismology) called the Greenland Ice Seismic Experiment (GreenISE) in 2015 and 2016 (*Schmerr* 2018). The data was filtered using a Butterworth band-pass filter between 40 and 250 Hz to remove the low and high frequency noise that potentially influence the picking of the first arrivals. This noise consisted of atmospheric (wind and blowing snow) and cultural artifacts. After filtering, the data are high quality enough to readily select the first arrivals of the various waves (Fig 2.1). The first arrival pick was defined as the first positive break from the zero amplitude of each seismogram.

To guide our picking process, particularly for the S-wave, a simple, 3-layer model was created. The model assumes a three layer case with a 15 m thick top firn layer, with a P-wave velocity of 3800 m/s and S-wave velocity of 1600 m/s, a 15 m thick middle aquifer layer, with a P-wave velocity of 3400 m/s and S-wave velocity of 2000 m/s and a 15 m thick bottom solid ice layer, with a P-wave velocity of 4000 m/s. The parameters used in the model were averages of the depth to the aquifer and thickness of layers from Table 1 and Montgomery et al. (2017). Predicted travel times are computed using a ray tracing approach, where take off angles from 0 to 90

degrees and expected refractions of waves from velocity changes are determined using Snell's law. Finding the range of takeoff angles that penetrate all layers, we find synthetic travel time curves can be found based on our parameters. We fit a two-term exponential model for the P-wave (P_{TT}) and S-wave (S_{TT}), whose coefficients were applied to the Greenland data, and used as the picking guide (Equations 3 and 4), where x is the distance from the source in m:

$$P_{TT} = 0.042e^{0.0031x} - 0.036e^{-0.019x} \tag{3}$$

$$S_{TT} = 0.084e^{0.0031x} - 0.073e^{-0.019x} \tag{4}$$

The uncertainty of the P-wave picks is less than 5 ms. Similarly, the S-wave arrival times were picked using the first positive breaks as well but with an uncertainty of about 10 ms (Fig. 2.1). The higher uncertainty in the S-waves is assigned due to the overlap of the P-coda and noise.

Surface wave dispersion was measured using the s*uphasevel* tool in Seismic Unix. Seismic Unix is an open source processing package developed at the Colorado School of Mines (*Cohen and Stockwell* 2013) and is a standardized tool in the analysis and processing of seismic datasets. The process *suphasevel* uses the transformation methods described by Park et al. (1998) to determine the phase velocity dispersion of the Rayleigh surface wave. This transformation method separates the frequency component of a given frequency and its arrival time information is preserved in the phase spectrum. The sum of the offsets in the arrival times are then taken after the phase shift at that frequency is determined, giving the phase velocity. Once the frequency window is determined, the offset-dependent phase

shift (or how much the first arrival deviates from the assumed phase velocity) is determined (*Park et al.* 2018). As parameters, we used a max frequency of 400 Hz and a minimum velocity of 350 m/s as the starting parameters and applied a Butterworth bandpass filter to the phase velocity processing to filter out noise lower than 10 Hz and higher than 250 Hz. The offsets of the wavefields of a given frequency in the frequency window are summed up to determine the coherence of the signal to the phase velocity. The more coherent, or self-similar, a signal is, the more confidence in the dispersion. We pick a range of frequencies that best envelop the peak velocities and respective frequency to create a dispersion curve (Fig. 2.1). In our automated phase velocity measurements sometimes overtone phase velocity, rather than the fundamental mode, is picked, which causes complications (Fig. 2.1C). The occurrence of overtones representative of the complexity of the subsurface, frequencies and receiver location (*Park et al.* 1998). The surface wave dispersion used in the inversion remove any overtones greater than 1 standard deviation of the mean to minimize the influence they may have on the models.

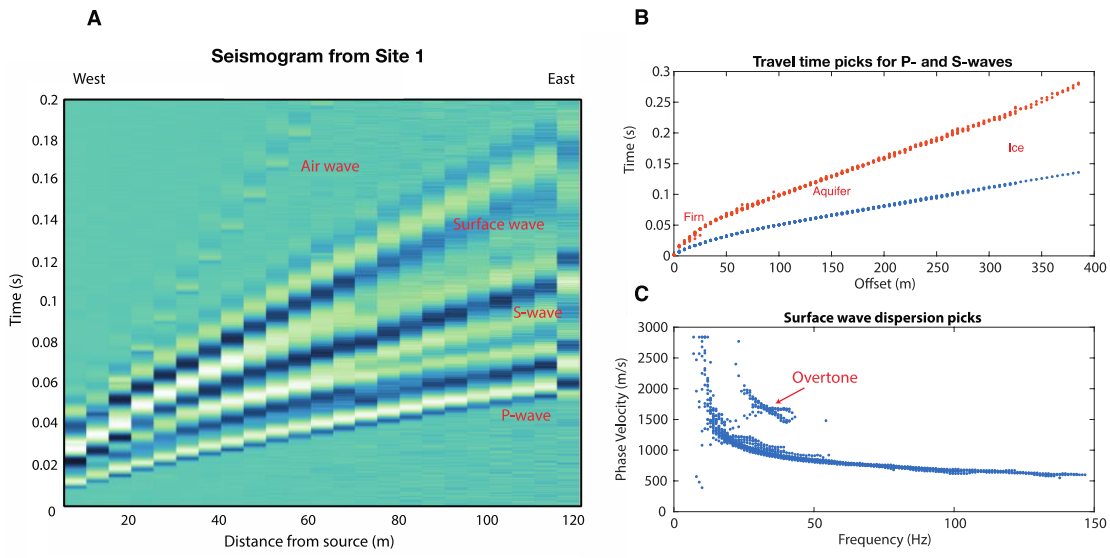

Figure 2.1: Example of our Seismic Data Set. A) Data from the vertical component geophones of site 1, located at 66.36 ° longitude and -39.53° latitude. The seismic source is 30 m from the first station. Each seismogram was normalized to the maximum at that distance. The different arrivals are labeled in red. **B)** Travel time picks for the P- (blue) and S-waves (orange). Expected layering structure from velocity changes labeled in red. Layer in which the waves are traveling through are labeled. **C)** Phase velocities from the surface waves dispersions.

2.2: Data Inversion

Traditional methods of inversions use optimization frameworks to search for the best fitting models. Here we implement a trans-dimensional Bayesian approach, using a reversible jump Markov chain Monte Carlo (rj-McMC) algorithm. We use a 1-dimensional, flat layer model to represent the subsurface structure. This process allows different parameters to be constrained individually via a joint inversion without specification of a starting model to invert for the velocity model, using P-waves, S-waves, and surface wave dispersions. The rj-McMC method is the sequence of models where the starting point is selected randomly, and the perturbations are dictated by the proposal probability distribution of the current model and a set of predetermined priors (*Bodin et al.* 2012).

The Bayesian method multiplies a likelihood function $p(\mathbf{d}|\mathbf{m})$, or the probability of the observed data, to the *a pirori* density of model **m** (p(**m**)) (Equation 5)

$$\text{Posterior, } p(\mathbf{m}|\mathbf{d}) \propto \text{likelihood, } p(\mathbf{d}|\mathbf{m}) \times \text{prior, p}(\mathbf{m}) \tag{5}$$

where **m** is the vector of model parameters and **d** is the vector defined from the observed data (*Sambridge et al*. 2013; *Bodin et al.* 2012). The trans-dimensionality of the model is proposed by creating Voronoi cells that act as nodes at pre-determined velocities. As new models are proposed, the boundaries between the cells adjust (Fig. 2.2). Our starting model for the V_S consists of 5 layers, with 5 boundaries at 2 m, 9 m 29 m, 44 m, and 55 m. The V_S of the first layer is .08 km/s, 1.2 km/s, 1.8 km/s, 2.1 km/s, 2.1 km/s. The V_P is about twice that of the V_S for each layer and the layering of V_P varies slightly to prevent possible errors in the inversion. We specify priors for the velocities between 0 and 4500 m/s while the layer depths are between 0 and 55 m.

The inversion begins with a random model and is allowed 3 million iterations to create an ensemble of 29000 accepted models that best represents the data collected (Figure 2.2). To allow the rj-McMC to converge to the observed data, we set a burn-in period of 100000 iterations. Once convergence occurs, the remaining number of iterations are collected into an ensemble of models. These models are collected every 100th iteration to increase the independency of the model (*Bodin et al.* 2012).

The starting model is proposed, perturbed, then the new model is accepted or rejected based on the misfit of the prior model (*Montgomery et al.* 2017; *Gao et al.* 2018). Since we are inverting for P-waves, S-waves, and surface waves, there is more

uncertainty with the addition of more parameters, thus more models are required to reduce the amount of misfit. These parameters are added as covariance matrices of data error. By inverting for the data noise, the data independently infers the contribution of the noise into the misfit (*Bodin et al.* 2012). In other words, extra parameters can be added as data matrices without having to adjust or scale the data to the misfit.

A primary assumption is that velocity is organized into constant layers with depth, with sharp contrasts in velocity, indicating a transition into a new layer. Based on the nature of P-waves, we anticipate sharp increases in velocity upon entering and exiting the aquifer structure (Montgomery et al. 2017). The S-waves should show a sharp increase in velocity occurring at the solid ice layer. The shear waves should be undeterred in the pore spaces filled with air and water but should be affected by the decrease in pore space from the compaction of snow into ice. Both P- and S-waves likely vary gradationally throughout the medium, but this is captured by multiple layers and are small relative to the larger material contrasts. The results from the inversion for the P- and S-wave inversions are shown in Figure 2.3 for site 1.

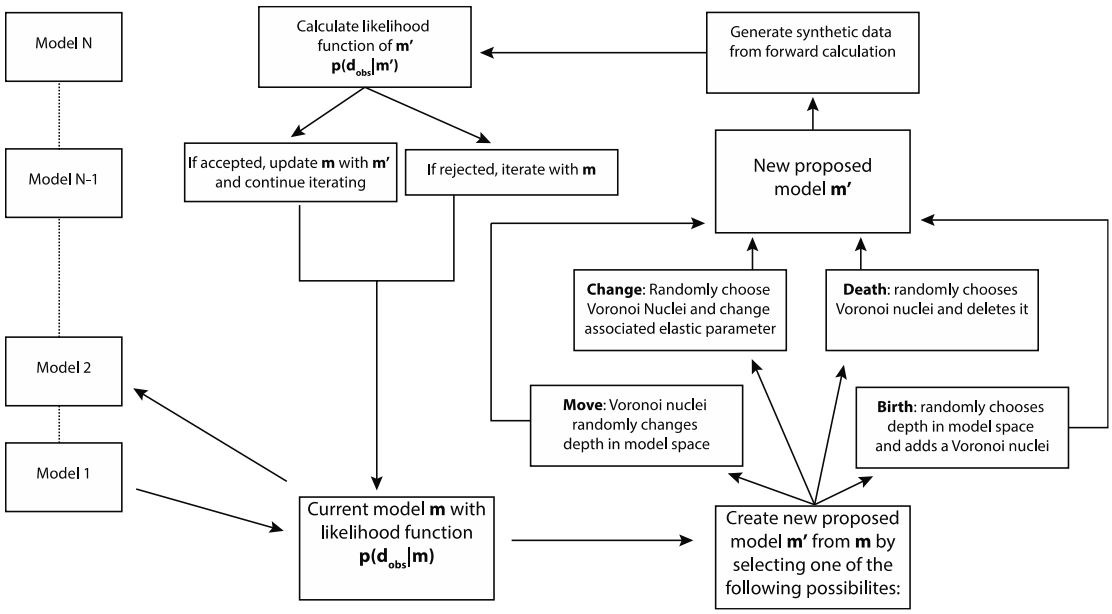

Figure 2.2: Schematic flow chart of the reversible-jump Monte Carlo Markov Chain. The model begins with model 1, runs *n* amount of iterations, then creates a new model until the Nth model is created. Modified from Gao and Lekic (2018).

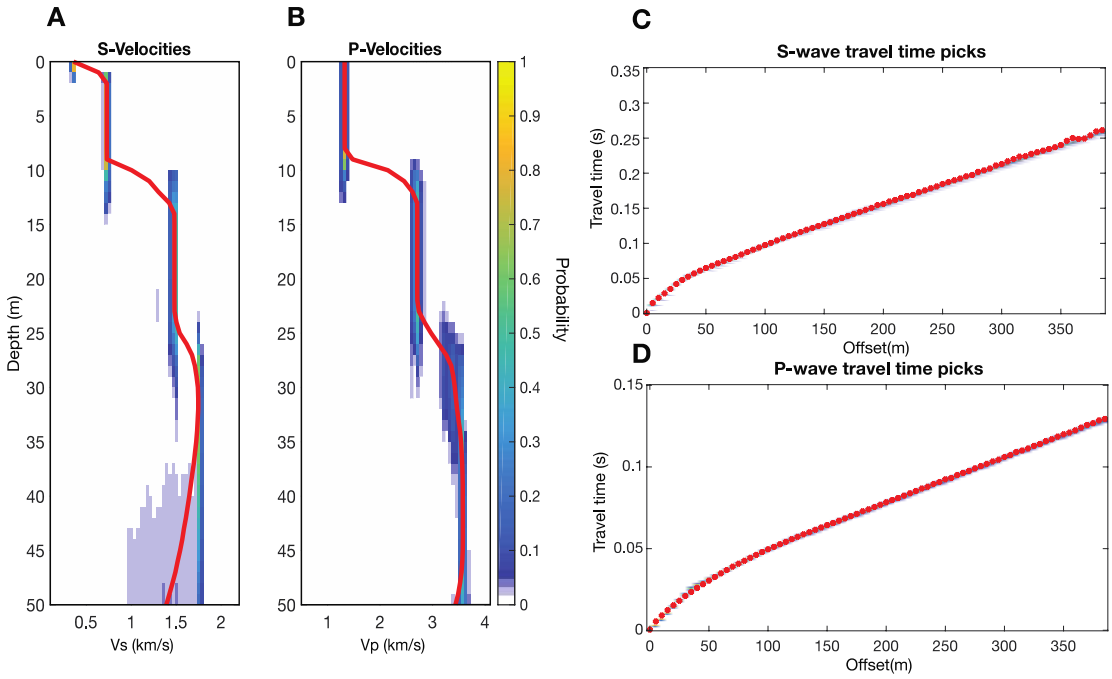

Figure 2.3: Inversion data from Site 1. A) S-wave inversions. The red line indicates the mean model based on the probabilistic distribution. **B)** P-wave inversion. The red line indicates the mean model. **C)** Travel time picks for the S-waves. The red dots indicate the physical picks. The misfit of the picks from the inversion are also plotted. **D)** Travel time picks for the P-waves with the misfit.

Chapter 3: Results

3.1: Joint Inversions

We conducted experiments using different combinations of the constraints (V_P, V_S, and surface waves) used in the reversible-jump Monte Carlo Markov Chain inversion to explore how well the combination of the constraints worked with one another. We first inverted P-wave travel time picks and the surface wave phase velocities (*joint inversion 1*), followed by inversions using P- and S-wave travel time picks and no surface waves (*joint inversion 2*), and inversions using all constraints (P- and S-wave travel time picks and surface wave velocities simultaneously) (*joint inversion 3*). Each combination of constraints in the joint inversion illustrate how different types of waves can either help or hinder the quality of the inversion. It should be noted that only the 2016 data set were used for the inversions, thus the exclusion of site 9 in the analysis. We exclude the 2015 data set as the resolution depth only resolves to 25-30 m, while the 2016 data resolves to 50-55 m (*Montgomery et al.* 2017). The uncertainties of the velocities were calculated to 1 standard deviation. The inversions, particularly in the deeper ice layers, have a much wider velocity probability distribution in the ensembles, due to the large uncertainty in the S-wave travel time picks.

The depths of the transitions can be found, with uncertainty, using the discontinuity probability/expectation, shown visually by the dotted lines in figures

3.1, 3.2 and 3.3, in conjunction with the inversions. The discontinuities are indicative of a change of velocity, as they portray the number of times the model had to reset until it was satisfied with the current model, as well as showing the likelihood of a transition change at a given depth. These discontinuities can be observed as velocity jumps in the inversions at each site.

The uncertainties in the depth were determined using the probability distribution of discontinuities from the ensembles (Figures 3.1-3.3). The depths between the troughs above and below the peak discontinuity are interpreted as the range of depths that a layer change is likely to occur (Figure 3.4). The uncertainties of the velocities were derived from the inversions by calculating the median of the ensemble between every velocity jump and finding the lowest and highest velocities of each layer (Figure 3.5). At deeper depths, the mean is influenced from higher uncertainties in the ensemble, so the median is more representative of the most likely velocity of each layer. Figures 3.4 summarizes the results for the depths and Figure 3.5 summarize the results for the velocities.

There is consistent layering between all inversions, which we can attribute to what we expect to see in the ice sheet. We define layer 1 (L1) as the firn, and in some instances divide it into sublayers (i.e layer 1A, layer 1B, etc.) due to lower velocities to those expected in the aquifer. Layer 2 (L2) and layer 3 (L3) are distinguished by their velocity and velocity jumps from the inversion results and are inferred as the considered the aquifer and solid ice respectively. The discontinuities between layer 1 and 2, and layer 2 and 3 are denoted as L1/L2 and L2/L3 respectively.

3.1.1: Joint Inversion 1- P-waves and Surface waves

When the P-wave travel time picks and surface waves are used as constraints in the inversion for P- and S-wave velocities, the recovered velocities have a high uncertainty (Fig. 3.1). The P-wave inversions show that L1A is strongly detected at 5.7 ± 4.3 m. However, the next observable velocity jump lies at 23 m ± 4.6 m depth, the transition between L2 and L3, falling near the base of the aquifer. This depth is about 5 meters shallower than the recovered depth to the base of the aquifer in Montgomery et al. (2017). The velocity jump expected from the water table does not appear in the P-wave inversions nor the surface wave shear wave inversions. There is much greater uncertainty between 5 m to 20 m, where the aquifer is expected to reside. Due to the coupling of both constraints in the inversion, the surface waves may not be resolving the aquifer well, as the top of the aquifer, it would lie around 5.7 ± 4.3 m. as indicated by the large uncertainty in the probability distribution in the shear waves (Fig. 3.1). The P- and S-wave velocities are shown in Table 2. The V_P of L1 is similar to the velocity of snow, or firn early in its development. The V_p of L2 is closer to firn (Table 1) than saturated firn. The V_P of L3 is comparable to the ice velocities of 3590 ± 133 m s^{-1} found in Montgomery et al. (2017). The S-wave velocities are expected to be approximately half of the P-wave velocities (Shearer 2009), however, inversion 1 indicates that the velocities of layers 1, 2 and 3 are ~ 47%, 41% and 37% of the P-wave velocity respectively. The slower velocities in the L2 and L3 are due to the large uncertainty in the inversion.

***Table 2**: P- and S-wave velocities of each layer and their uncertainties derived from the inversions*

	Inversion 1: V_P and Surface Waves		*Inversion 2: V_P and V_S*		*Inversion 3: V_P, V_S and Surface Waves*	
	P-wave Velocity (m s^{-1})	Shear wave velocity (m s^{-1})	P-wave Velocity (m s^{-1})	Shear wave velocity (m s^{-1})	P-wave Velocity (m s^{-1})	Shear wave velocity (m s^{-1})
Layer 1A	1151 ± 208	542 ± 206	1397 ± 183	745 ± 99.8	1315 ± 180	728 ± 116
Layer 1B	N/A	N/A	2269 ± 354	1146 ± 178	2142 ± 340	1031 ± 176
Layer 2	2344 ± 456	971 ± 260	2903 ± 198	1556 ± 139	2911 ± 175	1545 ± 98
Layer 3	3475 ± 287	1307 ± 103	3490 ± 294	1671 ± 189	3587 ± 204	1716 ± 132

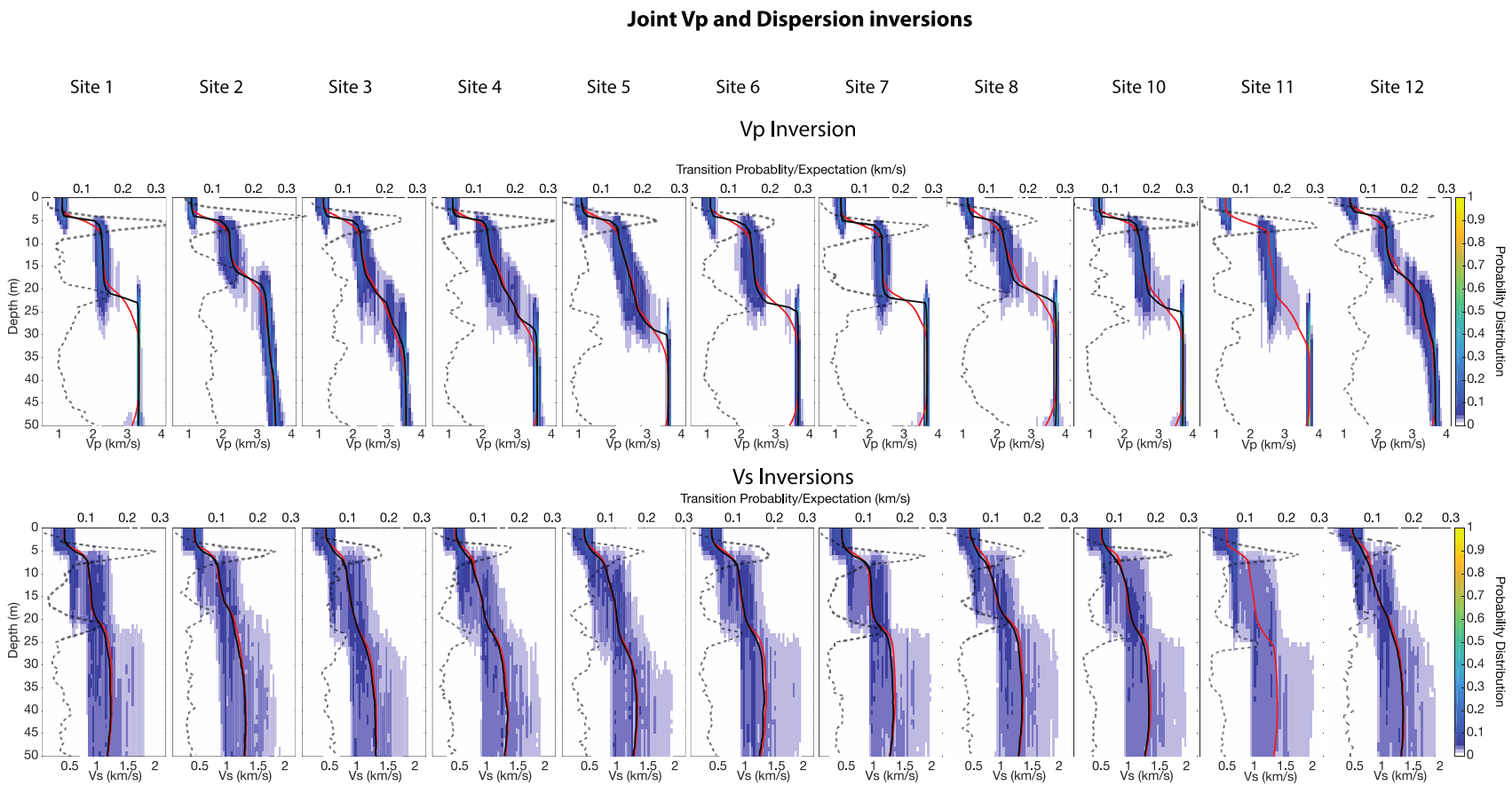

Figure 3.1: Inversion Data for all sites using P-wave travel time picks and surface wave dispersion (see section 3.1.1). The color bar on the right indicate the probability distribution of the ensemble of models. The probability distribution is derived from the ensemble generated for each inversion and indicates the probability of that velocity occurring at that depth. The closer the color is to yellow (1), the more likely that all models have that velocity. The bottom axes of each site indicate the velocity of the wave. The dotted grey lines indicate the probability distribution of discontinuities from the ensembles. **Top row)** P-wave inversions. **Bottom row)** S-wave inversions.

3.1.2: Joint Inversion 2- P-Waves and S-waves

Figure 3.2 show the results from inversion 2 for the P- and S-wave travel times across all sites on the Helheim glacier. The discontinuities and velocity jumps between L1/L2 and L2/L3 are observed across all sites. Sites 1- 4, 8 and 12 of the P-wave inversions show an extra velocity jump at L1A. This jump can be attributed to a large accumulation of ice lenses at these particular sites, discussed in more detail in the next chapter. The S-wave inversions all depict L1A in the upper 10m. There is an increase in uncertainty in the S-wave inversions below 30-40 m. We attribute this to uncertainty in the S-wave picks (See section 4.2).

The transition observed in the upper 2 m of site 12 in the P-wave inversions and all S-wave inversions is likely the compaction front from firn to ice. Sensitivity to this front is observed in the S-waves, and sparsely in the P-wave inversions. L1A is observed at sites 1-4, 8 and 12 in the P-wave inversion occur at a depth of 8 ± 3.4 m, and 7.2 ± 2.7 m in the S-wave inversion, giving an average depth of 7.6 ± 3 m. The transition L1/L2 occurs at 13.7 ± 4.3 m in the P-wave inversions occurs and 13.5 ± 4.0 m in the S-wave inversions, averaging out to 13.6 ± 4.2 m. The transition L2/L3 occurs at a depth of 27.9 ± 4.9 m in the P-wave inversion and 27.8 ± 4.2 m in the S-wave inversion, averaging to 27.8 ± 4.6 m. The transitional layer L2/L3 is consistent to the base of the aquifer of 27.7 ± 2.9 m from Montgomery et al. (2017), with the caveat being a higher uncertainty from our inversion results in the depths.

The thickness of the aquifer was determined at each site by subtracting the collocated measurements of the water table from the GPR radar depths presented in Montgomery et al. (2017) from the base of the aquifer calculated by our inversions.

We use the GPR depths because they were collected in situ at each site and provide better resolution to the top of the aquifer than our inversions, particularly upslope where more ice lenses may be present. These data are collected with a 400 Hz antenna and have a depth resolution of 2-3 cm. The average thickness of the aquifer using these constraints is 9.9 ± 4.9 m in the P-waves and 9.9 ± 4.2 m in the S-waves, yielding an overall aquifer thickness of 9.9 ± 4.6 m. Velocities from inversion 2 are shown in Table 2.

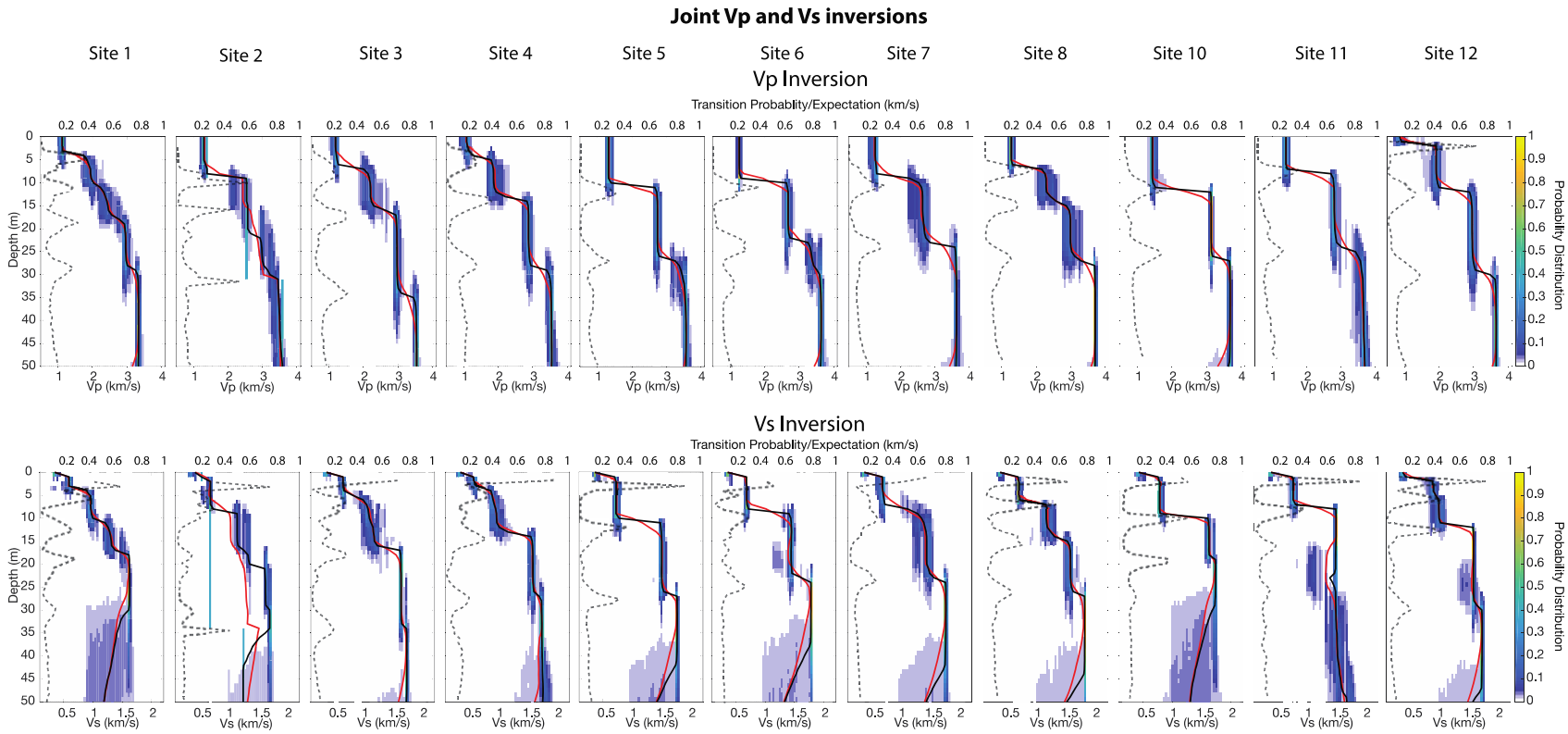

Figure 3.2: Inversion Data for all sites using P- and S-wave travel time picks (see section 3.1.2). The color bar on the right indicate the probability distribution of the ensemble of models. The probability distribution is derived from the ensemble generated for each inversion and indicates the probability of that velocity occurring at that depth. The closer the color is to yellow (1), the more likely that all models have that velocity. The bottom axes of each site indicate the velocity of the wave. The dotted grey lines indicate the probability distribution of discontinuities from the ensembles. **Top row)** P-wave inversions. **Bottom row)** S-wave inversions.

3.1.3: Joint Inversion 3- P-waves, S-waves, and Surface waves

The addition of the surface waves to the inversion provides another data set to refine the depths and velocities of the layers. In P-wave inversions, the only sites that do not have an additional sublayer, L1A, are sites 3-6. The S-wave inversions indicate another sublayer, Layer 1A, at all sites except sites 3-6. There is a velocity jump in the upper 2-3 meters present in most of the S-wave inversion sites, but this is not treated as an actual layer for consistency with the P-wave inversion comparison. It should be noted that the S-wave inversions, even with the inclusion of the surface waves, are more sensitive to the shallow structures than the P-waves. The shear waves at most sites consistently observe the presence of the ice lenses at shallow depths. The P-waves are not as sensitive to the upper 2-3 meters of each site as they have wavelengths about twice those of the S-waves.

The depths calculated from the inversions are comparable to that of inversion 2 conducted in section 3.1.2. The transition layer L1A/L1B lies at a depth of 4.8 ± 2.7 m in the P-wave inversion and 4.5 ± 2.3 m in the S-wave inversions. The transition L1/L2 occur at a depth of 13.1 ± 3.4 m in the P-wave inversion and 13.5 ± 3.4 m in the S-wave inversion. The transition L2/L3 occur at a depth of 27.8 ± 4.3 m in the P-wave inversion and 28 ± 3.6 m in the S-wave inversion. On average, transition L1/L2 occurs at 13.3 ± 3.4 m depth and transition L2/L3 lies at 27.9 ± 3.5 m depth. The thickness of the aquifer in this joint inversion is 9.9 ± 4.3 m in the P-wave inversion and 10 ± 3.6 m in the S-wave inversion, averaging to a thickness of 10 ± 4 m. The bulk velocities for inversion are shown in Table 2.

Systemic changes from site 1, located upslope on the Helheim glacier, to site 12, located downslope, can be observed. The velocities of the firn experience 29% increase from site 1 to site 10 but experience a velocity decrease from site 10 of 14% at site 11 and 24% at site 12. The increase in velocities could be a function of compaction of the firn, while the decrease in velocities at sites 11 and 12 may be due to a shallower water table and less snow/firn in this layer. The velocity of the aquifer at sites 1 and 12 are similar. However, there is large variability across all in the aquifer layer, possibly due to changes in water content at each site. The velocity of the ice increases systematically as sites traverse downslope. There is a 9.4% increase in velocity between site 1 and site 12, similar to the velocity change reported by Montgomery et al. (2017).

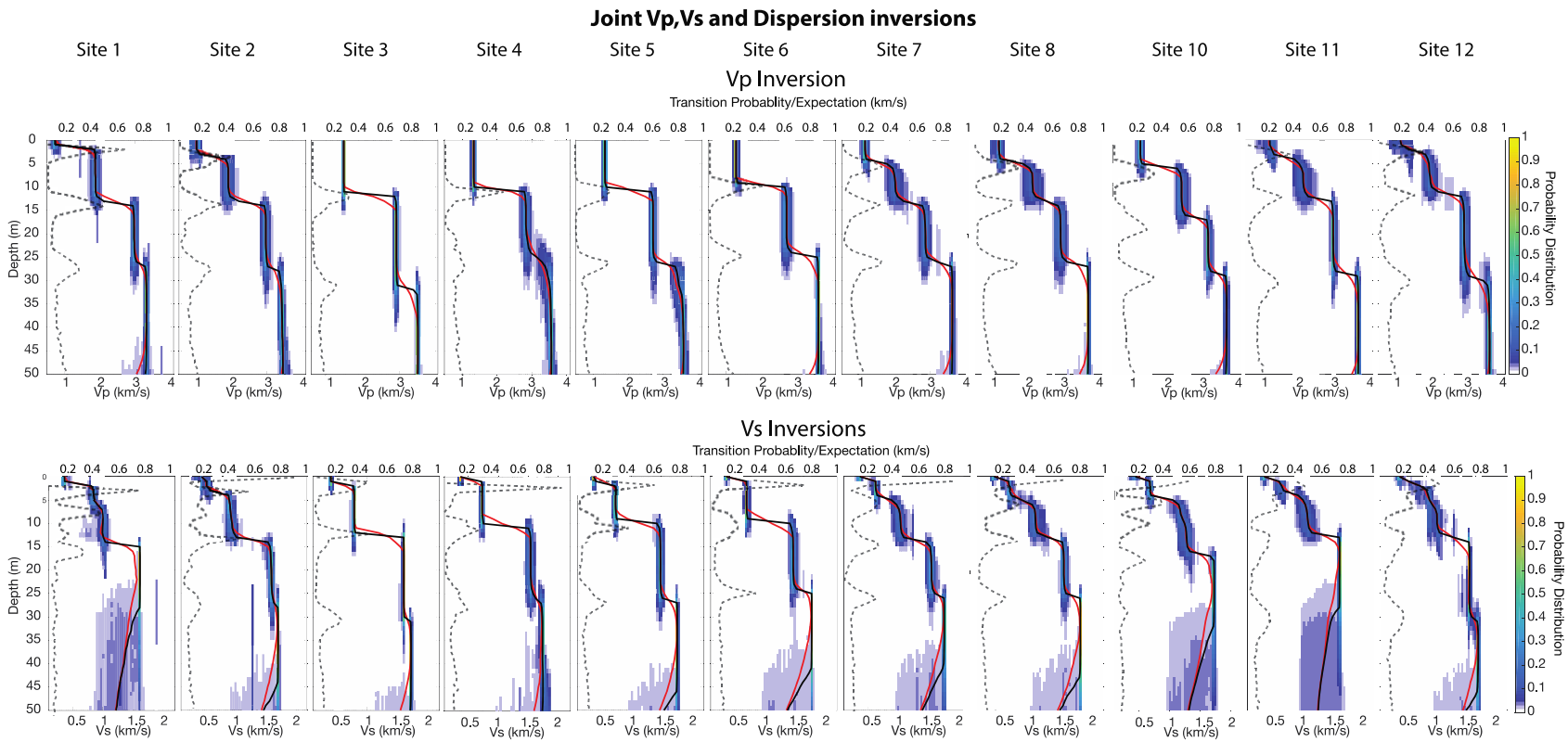

Figure 3.3: Inversion Data for all sites using P- and S-wave travel time picks and surface wave dispersion (see section 3.1.3). The color bar on the right indicate the probability distribution of the ensemble of models. The probability distribution is derived from the ensemble generated for each inversion and indicates the probability of that velocity occurring at that depth. The closer the color is to yellow (1), the more likely that all models have that velocity. The bottom axes of each site indicate the velocity of the wave. The dotted grey lines indicate the probability distribution of discontinuities from the ensembles. **Top row)** P-wave inversions. **Bottom row)** S-wave inversions.

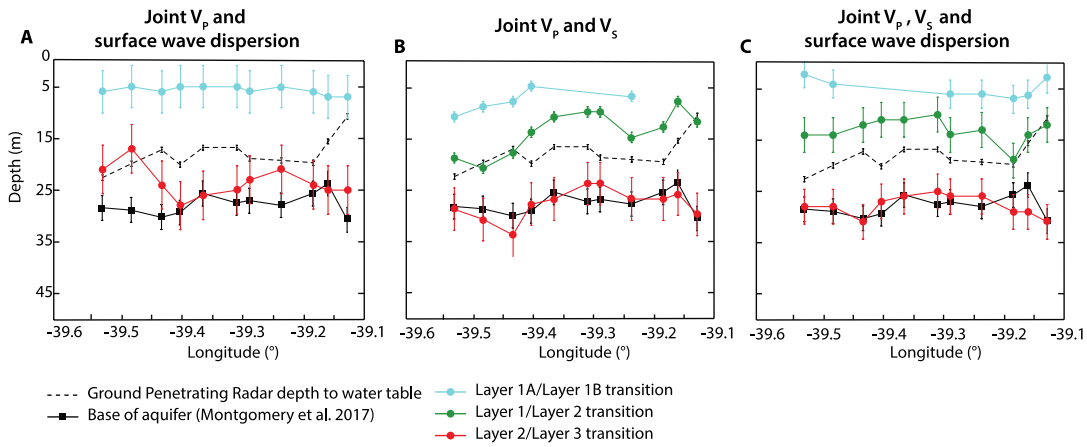

Figure 3.4: Depths of transitions between layers for the 3 inversion approaches. A) Joint V_P and surface wave dispersion (inversion 1). **B)** Joint V_P and V_S (inversion 2) **C)** Joint V_P,V_S, and surface wave dispersion (inversion 3). Error bars are calculated from taking the lowest and highest velocities from the median ensemble (Figures 3.1-3.3).

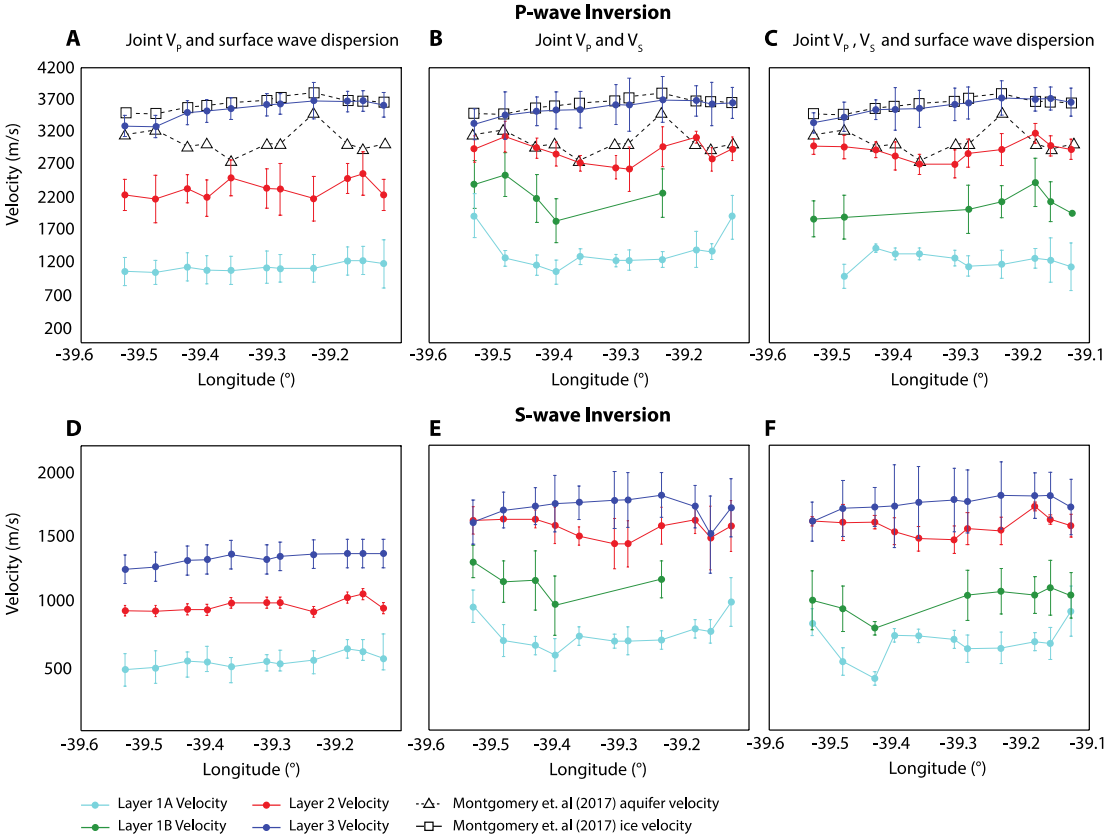

Figure 3.5: Velocity of different layers from the (A-C) P- and (D-F) Shear wave inversions. A,D) Joint V_P and surface wave dispersion (inversion 1). **B,E)** Joint V_P and V_S (inversion 2). **D,F)** Joint V_P,V_S, and surface wave dispersion (inversion 3). Error bars are calculated from taking the lowest and highest velocities from the median ensemble (Figures 3.1-3.3). Montgomery et al. (2017) P-wave velocities are also plotted.

3.2: Calculating Water Content and Volume

Perturbations in the aquifer layer velocity can be related to the liquid water content (LWC) in the aquifer. We use two different methods to calculate the LWC at each site. We first calculate the water content using Equation (6) (*Wyllie et al.* 1956), which describes the contribution of water content (ϕ) and the P-wave velocity ($V_{Paquifer}$) observed in the aquifer (*Montgomery et al*. 2017), under the assumption that pore space is saturated with water.

$$\phi = \frac{V_{P_{H_2O}}\left(\frac{V_{P_{ice}}}{V_{P_{aq}}} - 1\right)}{\left(V_{P_{ice}} - V_{P_{H_2O}}\right)} \times 100\% \tag{6}$$

The value for V_{PH2O} is 1450 m s^{-1} (Table 1), and V_{Pice} is derived from the measured velocity of ice below the inferred aquifer layer. We use this equation to compare the results from our inversions to the calculations from the previous study, where ϕ ranged from 8-24%. However, this method does not account for the empty pore spaces in the aquifer that are filled with air, rather than water. Thus, this method could be over estimating that amount of water present in the aquifer.

The next equation can be expected to account for the air present in the pore spaces, we use the S-wave velocities. Since seismic velocities are sensitive to the relative fraction of solid and liquid in a two-phased mixed system (*Montgomery et al.* 2017), we use Equation (6) to derive the bulk P-wave velocity of the aquifer,

$$V_{P_{Bulk}} = f_{air}V_{p_{air}} + f_{H2O}V_{P_{H2O}} + f_{ice}V_{P_{ice}} \tag{7}$$

where the f_{air}, f_{H2O} and f_{ice} refer to the volume fraction of the pore space of air, water and ice respectively. The f_{ice} can be rewritten as $(1-\phi)$, as it refers to the volume of ice

present, and ϕ refers to the bulk porosity. The same equation can be used for the S-waves (Equation 8).

$$V_{S_{aquifer}} = f_{air}V_{S_{air}} + f_{H2O}V_{S_{H2O}} + f_{ice}V_{S_{ice}} \tag{8}$$

However, S-waves do not travel through air or water, so their velocities are zero. Thus, the equation can be rewritten as:

$$V_{S_{aquifer}} = f_{ice}V_{S_{ice}} \tag{9}$$

Substituting $f_{ice} = (1-\phi)$, a new (ϕ) can be calculated, that should account for the water and air in the aquifer.

$$V_{S_{aquifer}} = (1-\phi)V_{S_{ice}} \tag{10}$$

$$\phi = 1 - \frac{V_{S_{aquifer}}}{V_{S_{ice}}} \tag{11}$$

The seismic velocities $V_{Saquifer}$ and V_{Sice} are derived from aquifer and ice velocities from the inversions in Sections 3.1-3.3 (Figure 3.5). Once a value for ϕ is calculated, the f_{H2O} can be determined by substituting the f_{air} as the difference between ϕ and f_{H2O} into Equation (7) to get Equations (12) and (13), where the fraction of water can be derived:

$$V_{P_{aquifer}} = (\phi - f_{H2O})V_{p_{air}} + f_{H2O}V_{P_{H2O}} + f_{ice}V_{P_{ice}} \tag{12}$$

$$f_{H2O} = \frac{V_{P_{aquifer}} + \phi\left(V_{P_{ice}} - V_{P_{air}}\right) - V_{P_{ice}}}{(V_{P_{H2O}} - V_{P_{air}})} \tag{13}$$

We then derive the water content (f_{H2O}) from our analysis other aquifer presented in figure 3.5. However, the presence of a low velocity zone (LVZ) is likely influencing the shear wave velocities that were measured by the inversions, as discussed in the next chapter. Thus, we will focus on the water content derived by Equations 6 and 11

to observe the differences in the methods. Note that these ϕ values are assuming the bubbles are filled with water only, thus can viewed as an upper bound of the water content in the aquifer.

For the joint V_P and surface wave inversions the LWC is > 25%, due to the poor delineation of the aquifer layer, while the other joint inversions are more similar to the LWC found by Montgomery et al. (2017). Comparing our results using Equation (6), the LWC of the V_P and surface waves dispersion joint inversion is 28-43%, the LWC of joint V_P and V_S inversion is 7-25%, and a similar amount (7-25%) is found in the joint V_P, V_S, and surface wave dispersion inversion. These ranges are similar to that of Montgomery et al. (2017). When we use the updated method from Equation (11), the water content averages from 22-33% in the V_P and surface wave dispersion inversion, 2-20% in the V_P and V_S joint inversion, and 5-17% in the V_P, V_S and surface wave dispersion joint inversion at sites where porosity is present. These ranges are less than the ranges calculated using Equation (6), indicating a porosity less than Montgomery et al. (2017).

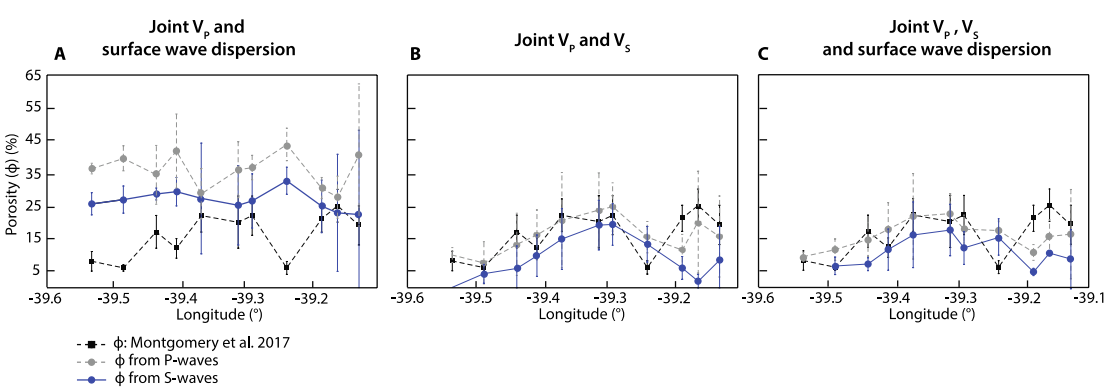

Figure 3.6: Porosity (ϕ) calculated from the inversions. The total water content using Equation 6 from Montgomery et al. (2017) is dashed for their results and ours, our values for LWC are indicated by the solid line. The calculations represented by the dotted lines use equation 6 to find water content. The solid blue line uses equation 11 to calculate water content. **A)** Joint V_P and surface wave dispersion inversion. **B)** Joint V_P and V_S inversion **C)** Joint V_P, V_S, and surface wave dispersion inversion. Error bars are calculated from taking the lowest and highest velocities from the median ensemble (Figures 3.1-3.3).

Using the water content calculated from each site, the storage capacity of the aquifer can be estimated by calculating the total mass off water per m^2 in the aquifer (Equation 14):

$$M_{H_2O} = \phi H \rho \tag{14}$$

where H is the thickness (m) of the aquifer, ϕ is the water content (%), and ρ is the density of water (1000 kg m^{-3}). We calculate the storage capacity using the LWC from Equations (5) and (10). Due to the omission of the 2015 data in our inversions, the storage capacity derived only accounts for sites 1-8, and 10-12, totaling 11 sites instead of the 22 sites used for storage capacity in Montgomery et al. (2017). Accounting for the sites used in our study, the Montgomery et al. (2017) average storage capacity is 1634 ± 983 kg m^{-2}. Using the LWC from equation 6, the average storage capacity 1565 ± 769 kg m^{-2}, while the LWC from Equation (11) yields an average storage capacity of 1082 ± 443 kg m^{-2}. The storage capacity for each site using the three data sets is shown in Figure 3.7. A general increase in the storage capacity can be observed from site 1 to site 12, as the system moves downslope.

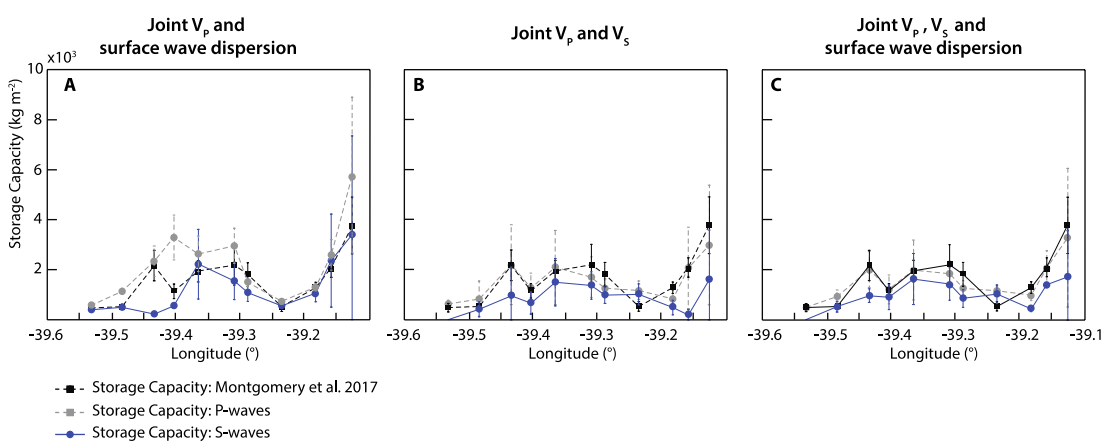

Figure 3.7: Storage capacity calculated from inversions. The storage capacity derived from equation 6 (dotted line) and equation 11(solid). **A)** Joint V_P and surface wave dispersion inversion. **B)** Joint V_P and V_S inversion **C))** Joint V_P, V_S, and surface wave dispersion inversion. Error bars are calculated from taking the lowest and highest velocities from the median ensemble (Figures 3.1-3.3).

Chapter 4: Discussion and Conclusion

Our study provides a quantitative method for measuring the dimensions of the aquifer and its water content. Here we discuss the reliability of these methods. Furthermore, based upon our study of S and surface waves, we hypothesize the presence of a low velocity zone, and discuss how the aquifer can produce such a feature for the shear waves. To examine this hypothesis, we first look at synthetic seismograms to understand the behavior of the seismic waves and its interactions with the aquifer. We then compare results from our inversions to cores and hydrological data collected on the Helheim glacier to better understand the geophysical signals validated structures within the firn aquifer. Miller et al. (2017) extracted ice cores *in situ* from sites 6, 7, 8, 10, and 12 of our study area and measured the density of each core. Furthermore, sites 7, 8, and 12 had specific conductance and specific discharge measurements taken to measure the flow of water within the aquifer. Since the cores were extracted at similar sites to where the seismic data was collected, we can

directly validate the results of our inversions against the background structure and ground truth our interpretations.

4.1: Implications of a Low Velocity Zone

An experiment conducted by Helgaard et al. (2003) shows that V_S decreases with increasing pressure in a three-phase mixing model (consisting of ice, water, and sediment), while V_P is continuously increasing as a result of ice grains bonding from the compaction. S-wave inversions show a large uncertainty near the greatest depths of the firn system. The S-waves in our data are weaker at greater distances, increasing the difficulty of picking of their first arrivals. This translates to greater uncertainty at depths below the aquifer, with the mean velocity of the ensemble skewed by poor fits to these outlier data. One possibility is that surface waves may be overprinting the S-waves, as energy from the surface waves is usually stronger than the energy of the S-waves. With the velocity of the surface waves being about 90% of the S-waves, our picking may have selected surface wave moveout. Alternatively, near surface reflections and reverberations of P-waves or S-waves would mimic the moveout of direct S-waves and contaminate our S-wave travel time picks. If a low velocity zone is present in the aquifer layer, direct S-waves would experience a shadow zone and violate our assumption of velocity increasing with depth in the rj-McMC.

These explanations elucidate the observed V_P/V_S ratio that we found in the rj-McMC. As stated earlier, the V_P/V_S ratio is typically used as an indicator for the presence of fluid in a saturated rock, as it is dependent on the porosity and the fluid pressure (*Lee* 2003). Thus, calculating the V_P/V_S ratio should provide further evidence for the presence of water. We found an average V_P/V_S ratio for firn layer 1

of 1.86, 1.99 in firn layer 2, 1.84 in the aquifer layer, and 2.04 in the ice layer. Firn layer 1A and the aquifer have very similar ratios, while firn layer 2 more closely resembles the V_P/V_S ratio of 1.95 ± 0.04 observed on the Rutford ice stream (*Smith et al.* 2015), more indicative of ice. This is opposite of what is expected when comparing the V_P/V_S ratio of a saturated medium, for example, a saturated rock, where V_P/V_S is greater than 2. One reason could be because the ice lattice is stiffer than water and air, thus increasing the compression and shear of the waves as a function of the water-to-ice ratio (*Zimmerman and King* 1986). However, when we calculate the probable error of the V_P/V_S ratio of each site, the uncertainty is too large to accurately distinguish the ratios between layers (Figure 4.1). Given this large error, we instead examine the V_P and V_S velocities individually.

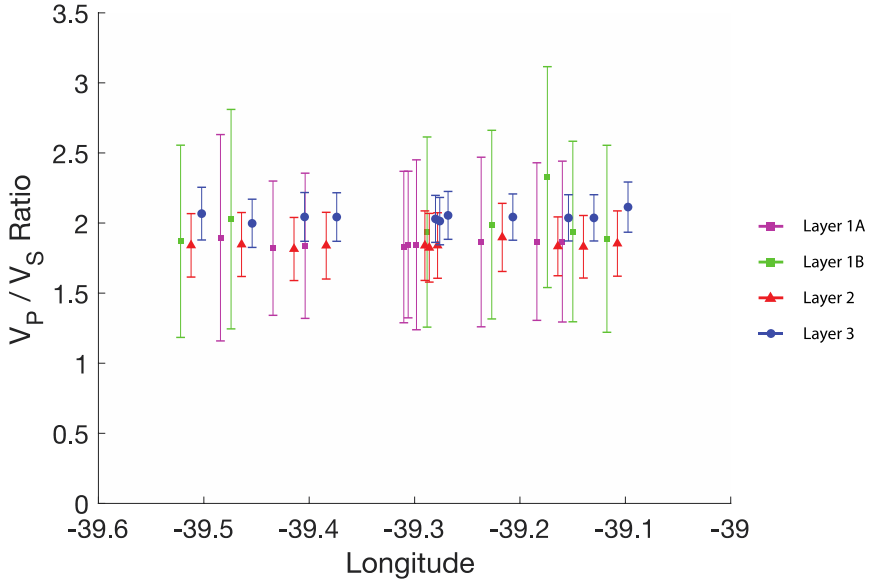

Figure 4.1: V_P/V_S ratio calculated from Joint inversion 3 for the layers in our study. The V_P and V_S were divided against each other for each layer at each site. Error bars are calculated from taking the lowest and highest velocities from the median ensemble (Figures 3.1-3.3). The layers are offset by 0.01° longitude to compare the dataset.

By using Equation 13, we can calculate the expected velocity range needed in a case where there is no water content in the aquifer ($f_{H2O} = 0$) and a case where all of the porosity available is filled with water ($f_{H2O} = \phi$) (Figure 4.2). For this model, we assume the V_P is 3700 m s^{-1}, V_{Pair} is 340 m s^{-1} and the V_{PH2O} is 1450 m s^{-1} (Table 1). The calculated water content derived from the S-waves lies outside the threshold set by our water content model, implying that Eq. 11 is underestimating pore space. To reach this threshold, we must increase porosity by a factor 2-3 to produce reasonable estimates for V_P in the aquifer using the S-wave constraint of ϕ. Here we present synthetic modeling to investigate the effects of an LVZ on the shear waves. This discrepancy is consistent with lowered S-wave velocities in the aquifer that is not resolved in our data analysis and would lead to the unexpectedly low V_P/V_S for the aquifer layer.

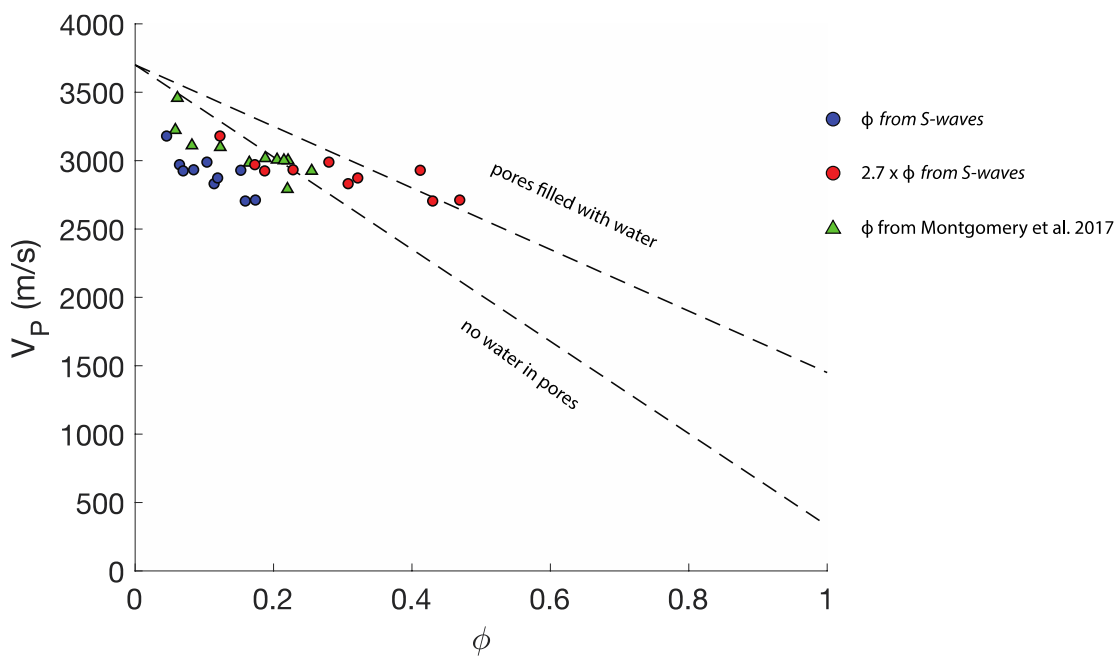

Figure 4.2: V_P vs water porosity (ϕ) derived from equation 11. The dotted lines represent the extreme cases of water content filling the pore spaces. The blue circles are the measurements from equation 11 for joint inversion 3.

The red circles indicate the water content derived from S-waves, multiplied by a factor of 2.7. The triangles indicate the water content reported by Montgomery et al. (2017).

4.1.1: Synthetic Modeling

We use Specfem2d (*Tromp et al.* 2008) to create synthetic seismograms to investigate the behavior of the seismic waves (Fig. 2.4). Specfem2d is a spectral element forward modeling software that simulates seismic wave propagation in a poro-elastic media in two dimensional or three-dimensional mesh. The forward modeling allows us to simulate the changes in velocity we expect to see, given the densities and velocities observed in glacial system (Table 1). We selected the base model geometry used for the synthetic forward modeling from site 11 as it is constrained from GPR (*Legchencko et al.* 2018), seismic (*Montgomery et al.* 2017), and ice core data (*Miller et al.* 2017). Our model has 24 geophone stations and a seismic source with a dominant frequency of 150 Hz at the surface and 10 layers to represent the gradational changes in the glacier that we expect to observe (Fig 1.2). The geometry of the synthetic survey is identical to the survey seen in Figure 1C.

Six different models are tested to observe differences in the effects of attenuation and the presence of a low velocity aquifer layer (Fig. 4.3). The quality factor, Q, is representative of the attenuation of waves, where higher Q indicate lower attenuation and low Q indicate high attenuation. Q factors of 5, 10, and 50 were used to represent low, medium and high attenuation, respectively. Models 1-3 have no low velocity zone, where model 1 has high attenuation across all layers, model 2 has uniformly low attenuation, and model 3 has Q=5 for the top 3 layers, representative of firn, Q=10 for the middle 3 layers , representative of the aquifer, and Q=50 in the

bottom 4 layers, representative of ice. The goal of these synthetic models is to study the behavior of the S-waves and surface waves and determine how reliable the S-waves and surface waves are in the inversions. Velocities in models 1 and 4, 2 and 5, and 3 and 6 are identical to one another, with the only difference being the presence of a low velocity zone in the aquifer, where we decrease the S-wave velocity from 1550 m/s to 1100 m/s. Shot locations occur at 30m intervals beginning at the first station, and extend to 240 m from the first station, recreating our station geometry in the refraction experiments.

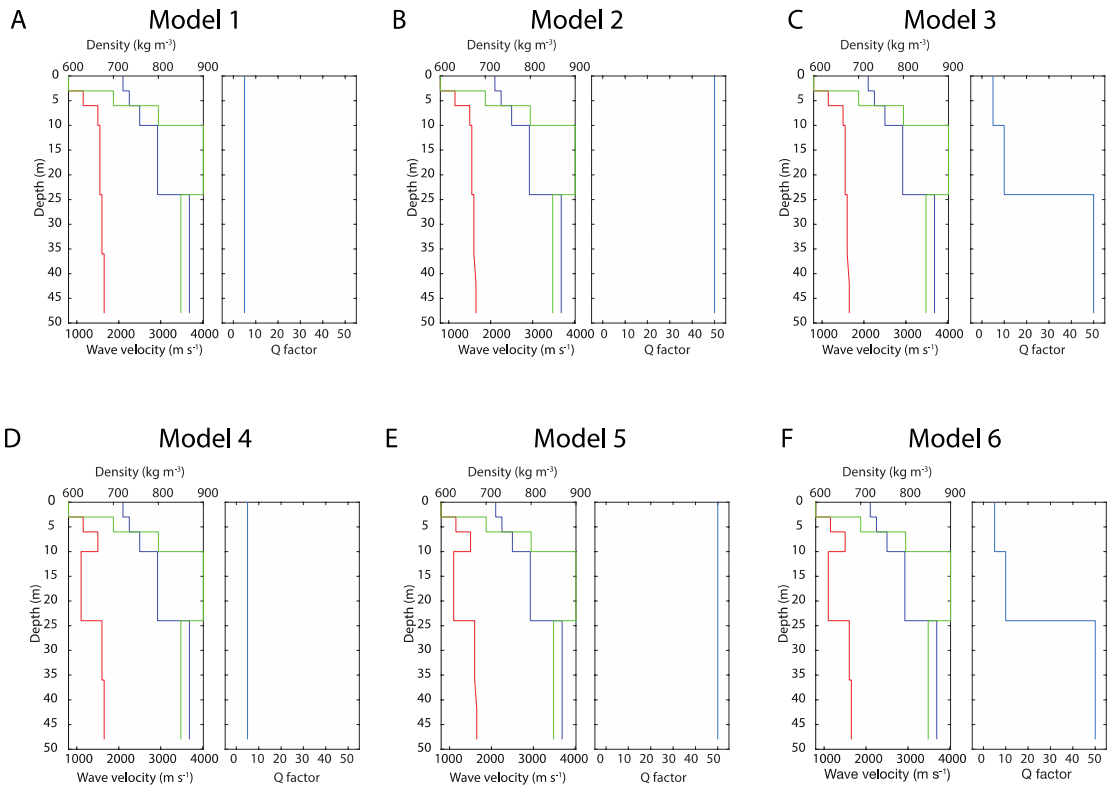

Figure 4.3: Models of firn aquifer structure explored in our synthetic surveys. A-C) Models with no low velocity zone. **D-F)** Models with a low velocity zone. The panel on the left shows the velocity and densities for each model. The blue line depicts the P-wave velocity of the model while the red line depicts the S-wave velocity (m s^{-1}). The green line depicts the density used for each layer (kg m^{-3}). The panel on the right depict the Q-factor for each layer.

4.1.2: Synthetic Seismograms

The synthetic data allow us to observe the behavior of the waves as we can control parameters such as the degree of attenuation in each layer or the velocity of each layer. We first compared the cases of high attenuation (Q=5) in all layers to the data from site 11 (Fig. 4.4 A,E,I). There is a large residual between the model with and without a low velocity zone. These residuals can be classified into 3 primary types: 1) reverberations in the near surface layers that are enhanced by the presence of a LVZ, arriving after the direct and refracted P-waves, 2) reverberations in the near surface layers that arrive near the predicted S-waves that are enhanced by the LVZ, and 3) additional energy in the surface wave field, presumably associated with the LVZ (Fig. 4.4: I-K). Multiples follow the P-waves as a coda can be observed in synthetic data, as well as the data collected in Greenland, indicating the likelihood of the reverberations caused by the impedance contrasts of the P-waves at the top of the aquifer. Due to the changes in the velocity and density, not all energy in the seismic waves gets transmitted in the next layer. Some of the energy is reflected off of the impendence contrast at the boundary, particularly when the density and velocity of the underlying layer is greater than that of the overlying layer. The low attenuation models (Q=50) has high frequency surface waves not seen in the data. Only the layered model produces waveforms similar to the observed data. Attenuation of the S-waves and surface waves are observed in both cases, with more attenuation present in the low-velocity zone models. The data from site 11 show a clear arrival of both the S-wave and surface waves.

We then compare models 2 and 5, where all layers have low attenuation (Q=50) (Fig. 4.4: B,F,J). In this scenario, P-waves experience the reverberations previously observed, but to a lesser extent. The S-waves and surface waves are more prevalent due to less attenuation. The shear waves appear to experience greater reverberations. One possible explanation could be that the head wave converted from a P-wave to an S-wave upon reflection of the aquifer and continued as an S-wave because it could not be transmitted into the liquid aquifer layer. Similar reverberations can be observed in the surface waves as well. The presence of the low velocity zone appears to limit the distance of reverberations in the S-waves to 70-110 m, but the effects on the surface waves are similar. The residual between models 2 and 5 highlight a subtle increase in arrival times influenced by the low velocity zone. This corresponds to a dip in amplitudes of the observed seismic wavefield between 90 and 110 m.

Lastly, we compared models 3 and 6 (layered attenuation) with the data from site 11 (Fig. 4.4: C,G,K). This scenario mimics the subsurface expected in the real data. The P-waves in the synthetic models show that the reverberations still occur. However, the S-waves and surface waves appear to attenuate more, likely due to the high attenuation used in the firn layer. The presence of a low velocity zone makes it difficult to differentiate between the S-waves and surface waves. However, the real data shows that there is a clear separation between all the waves. The synthetic modeling indicates that the body waves are subject to reverberations, an effect that would make unique picking of the S-waves difficult.

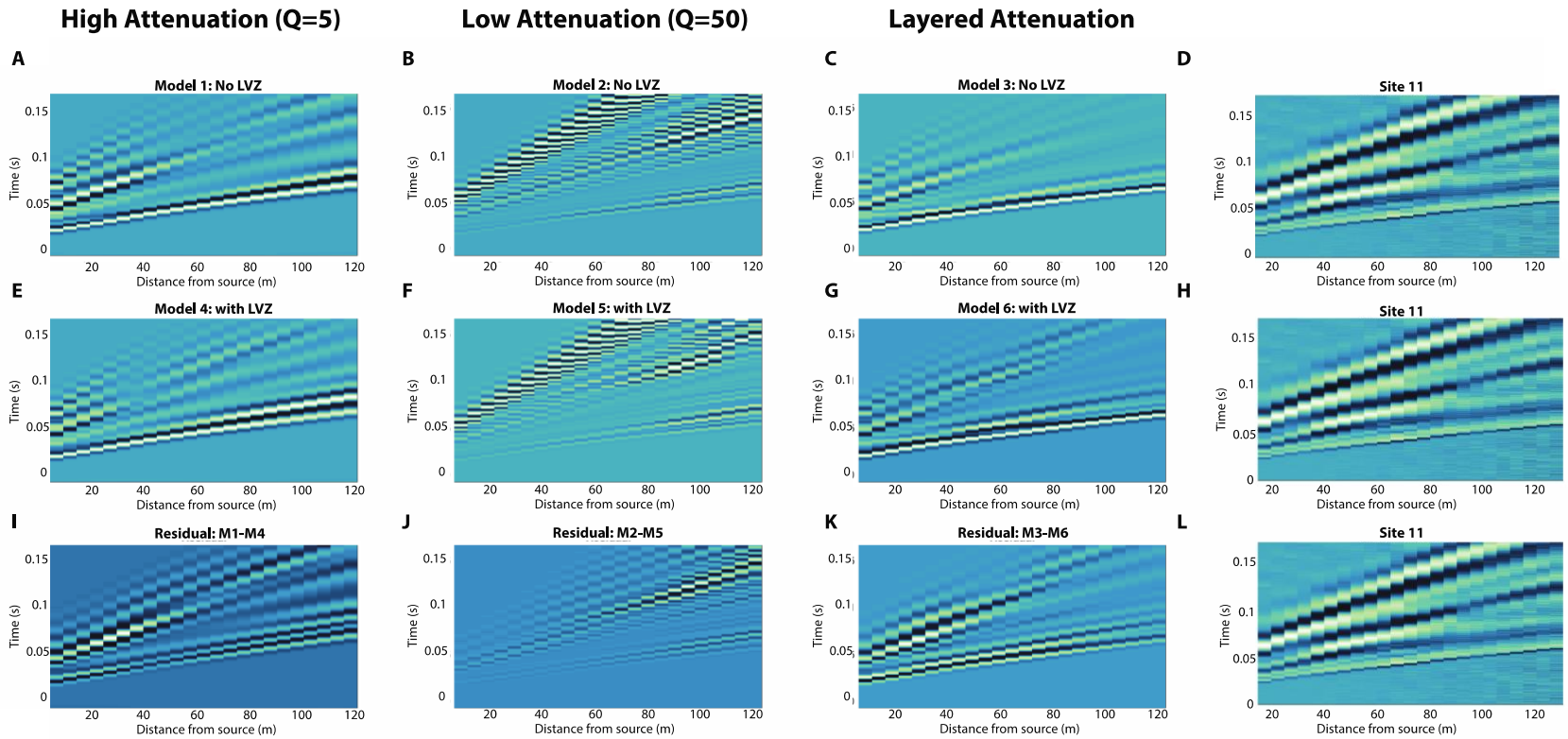

Figure 4.4: Synthetic Seismic Data Comparing all 6 models to Site 11. Source of seismic data is 30 m from the first station. **A-C)** No low velocity zone present. **E-G)** Low velocity zone present. **I-K)** Residual data between models 1 and 4, 2 and 5, 3 and 6 respectively. The residual is acquired by subtracting the difference between the amplitudes to find where the two models differ. **D,H,L)** Data from site 11 used for comparison to synthetic data.

4.2: Reliability of Joint Inversions

In the previous section, we examined the presence of an LVZ and how it would affect the S-wave arrival times used in our survey. In this section, we compare the different joint inversions and how additional constraints on the data aid (or hinder) the inversions. A primary component is how the surface and body waves sample the firn structure. The P and S body waves experience less changes in frequency and less dispersion of waves than their surface wave counterparts (*Kanamori and Anderson* 1977). The hammer source creates body waves at a frequency of 150-200 Hz, we expect the body waves to retain most of the emitted frequency. Given the velocities given in Table 1, and a frequency of 150-200 Hz, the wavelength of the P-waves has a resolution depth of 14-20 m, while the S-waves are around 7-9 m. Surface waves are sensitive to the phase velocity (Fig. 1.2C), and thus observed dispersion is sensitive to both changes in velocity and attenuation. High attenuation is present at the shallow surface structure and decreases for deeper structures. As a result, surface waves sensitivity to structure is variable throughout the subsurface. Below we discuss how different combinations of *Joint Inversions 1, 2* and *3* details affect the sensitivity of the inversion, and which is likely the most useful at detecting subsurface structure.

Joint inversion 1 includes only surface waves and P-wave travel times as constraints, thus is sensitive to the large variability in attenuation across the aquifer, as indicated by the use of data only up to 1 standard deviation in all data sets. The sensitivity of the P-waves to subsurface structure starts at about 14 m, while any subsurface structure shallower than 14 m should be resolved by the surface waves.

For *joint inversion 1*, the seismic velocity jump between L1A and L1B at 5.7 ± 4.3 m is likely to be a secondary, more compacted layer of firn, since this depth is more similar to the L1A/L1B transition of the other inversions rather than the depth of the aquifer. The velocity in the firn layer resembles the upper bound of that found in snow (Table 1), rather than firn. The velocity in the interpreted aquifer layer is more similar to the firn, rather than the expected velocity of saturated firn. The velocity in the ice from this inversion agrees with the ice velocities of the other two inversions. However, the L2/L3 transition occurs at a shallower depth of 23 ± 4.6 m, roughly 4 m above the other calculated aquifer bases. The sensitivity of the P-waves allows for the detection of the bulk structure, as shown in Montgomery et al. (2017), but the larger wavelengths from the surface waves are likely sensing structure prior to reaching the aquifer, creating more attenuation and disparity in the waves at depth. Overall, using solely surface waves and the P-waves in a joint inversion is not reliable due to the large uncertainty caused by the data of the surface waves.

Joint inversion 2 uses the P-waves and S-waves as the main constraints in its inversion, while *joint inversion 3* uses the P- and S-waves and surface waves in the inversion. The resolution depth from the S-waves is about 7 m, so *joint inversion 2* should be able to resolve any feature greater than 7 m into the subsurface and below, while *joint inversion 3* should resolve the upper 7 m from the surface waves, providing a unified picture. *Joint inversions 2 and 3* have very similar velocities for the firn, aquifer and ice layers (Table 2). However, joint inversion 2 has ~30% larger uncertainty than joint inversion 3. Based on Table 1, the velocities in L1A of both *inversion 2 and 3* are consistent with a transitionary interface between snow and firn,

with larger pore space toward the surface. The velocities in layer L1B could be interpreted as firn that has undergone more compression, and reduction of porosity. Our velocity ranges in the aquifer are consistent with those found in the aquifer layer of Montgomery et al. (2017), while the velocities from layer 3 agree with velocities of solid ice of ~3400-3800 m s^{-1}. As both *joint inversions* 2 and 3 are reliant upon S-waves, and we identified the possibility of a shadow zone within the aquifer layer, the results for deeper structure are unreliable for the S-wave structure without the surface wave constraints.

The biggest difference between the two inversions is the depths between L1A and L1B. In inversion 2, this transition depth occurs at 7.6 ± 3 m, while in inversion 3, this transition occurs at 4.8 ±2.7 m. The overlying firn layer are observed at sites 1, 3, 4, 8 and 12 in the P-wave results of *inversion 2*, while the P-wave results of inversion 3 find that sites 1, 2, and 7-12 have an observable, overlying firn layer. The seismic velocity jump that occurs at 13.6 ± 4.2 m in inversion 2 and 13.3 ± 3.4 m in inversion 3 can be interpreted as the top of the aquifer in both inversions. However, the GPR measurement taken *in situ* indicate that this velocity jump is much shallower than the known depth to the water table. The difference between the two presumed depths to the aquifer in sites 1-9 are ~6.5 m on average, and at sites 10-12, the difference is ~ 1.6 m on average. The velocity jump at 27.8 ± 4.6 m in inversion 2 and 27.9 ± 3.5 m in *inversion 3* is inferred as the base of the aquifer, consistent with the pore closure depth of 27.7 ± 2.9 m reported by Montgomery et al. (2017) and base of the firn layer of 27.7 ± 4.4 m reported by Robertson and Bentley (1975). The base of the aquifer, or the pore closure depth, is controlled by the thermodynamics of the ice,

where melting requires the surrounding ice to absorb heat, and freezing requires the ice to release heat (*Mishima and Endo* 1980). Since the glacier is laterally relatively uniform, there is a similar amount of snow and firn from site to site. Thus, similar pressures and temperatures form a pore closure depth at a semi-constant depth across the study area, which we observe in our joint inversions, similar past studies.

The presence of ice lenses, on the order of decimeters to meters thick reported in Miller et al. (2017), indicate that ice stratigraphy could be influencing the seismic velocity recovered by the inversions. Figure 4.5 shows the comparison of our P-wave inversions at sites 6-8, 10 and 12 to the local stratigraphy. The increase in the fraction of ice lenses occurs near the velocity jumps observed in the inversion data. The velocity jump near the top of the aquifer in sites 6-8 does not correlate with the observed depth. Rather, the velocity jumps associated with the presence of large ice lenses, since ice and highly compacted firn have higher bulk velocities than uncompacted firn. Wherever increases in density in the ice cores are present, velocity jumps in the inversion data can also be seen. At sites 6, 7 and 8, the presence of water in the firn increases the density of the system, but the amount of ice lenses is 5-8% in the upper firn layer, to 23-24% in the lower firn and increases again 22-37% in the aquifer layer. At sites 10 and 12, the density increase, GPR depth, and the velocity jump of the inversion are observed at the top of the water table. This layer has ~10-17 % ice lenses but is relatively thin compared to the other sites as there is only 1 firn layer in the inversion. However, the ice core at site 10 indicates a thick ice lens at 15 m depth, which could also cause the jump in velocity observed at this depth.

The interpreted seismic base of the aquifer coincides with the occurrence of bubbly ice and clear ice in the ice cores at sites 6, 7, 8 and 10, where the ice lens percentage increases to ~76.4-100 %, thus indicating the pore closure depth or freeze out point. At sites 6, the seismic base of the aquifer occurs at 25 m depth. At site 12, the seismic base of the aquifer occurs between two intervals of clear and bubbly ice. The hydraulic conductivity from Miller et al. (2017) provides another indication to the base of the aquifer and where pore closure occurs. At sites 7 and 12, the saline solution introduced by the method would accumulate above the solid ice and is measured as the solution is diluted by the fresh water flowing through the aquifer. The large concentration of saline water at the base of the aquifer is comparable to the seismic bottom depth at these sites (*Miller et al.* 2017). However, there is no saline water accumulation at site 8 due to an increased and continuous flow of water (*Miller et al.* 2017). Given all the information together, there is agreement in the seismic bottom of the aquifer, which lies, on average, at 27.9 ± 3.5 m.

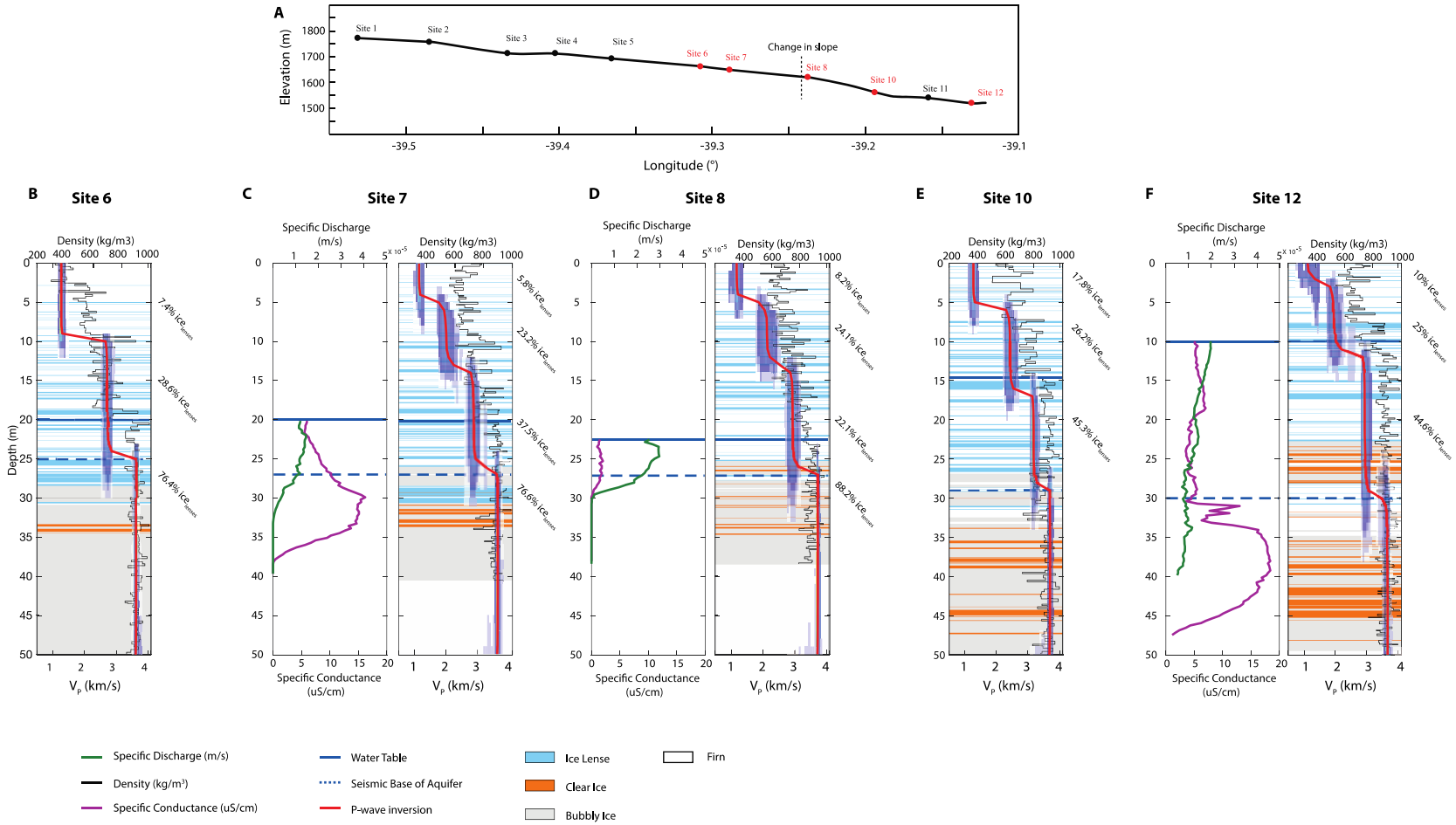

Figure 4.5: Comparison of P-wave inversion results to ice cores from Miller et al. (2017). A) Elevation at each site. The surface topography is obtained from a Worldview-1 (DigitalGlobe©). **B-F)** Joint V_P,V_S, and surface wave dispersion inversion for P-waves plotted above the ice core data for sites 6, 7, 8, 10, and 12 from Miller et al. (2017). Sites 7, 8 and 10 also show specific discharge and conductivity from their study. Percentages of ice lenses for each observable layer from the seismic data are also shown.

The average thickness of the aquifer of inversion 2 is 9.9 ± 4.6 m and 10 ± 4 m in inversion 3. The uncertainty the aquifer is ~13% thinner in inversion 3. Both thicknesses are about 2 m thinner than the 11.5 ± 5.5 m stated by Montgomery et al. (2017). The large uncertainty in thickness is a function of the increase in the aquifer seen downslope. At site 12, the aquifer is 20.3 m thick, while the thickness of the aquifer at sites 1-11 does not exceed 14 m. The inclusion of surface waves in inversion 3 as a constraint reduces the uncertainty in the velocities by ~30% and reduces the uncertainty to the bottom of the aquifer by ~15%.

As shown in Figure 4.6, the velocity of the waves is more dependent on the amount of ice present rather than the presence of the aquifer, but there is still an observable influence of the presence of liquid water on the seismic data. In the aquifer layer (20-40% ice lenses), there are velocities in both the P-waves and S-waves that are above and below the line of best fit, likely due to the water. When taking this into consideration, this returns to our arguments for why the presence of water does not increase the V_P/V_S ratio as expected. The S-waves that were picked are likely reverberations of the P-wave. The arrival of the S-waves may be influenced by the presence of a low velocity zone from the aquifer, so they may not be present in our data set. There is less than a 170 m s^{-1} difference between the S-waves of the aquifer layer and ice layer in joint inversions 2 and 3. This increase is most likely due to compaction.

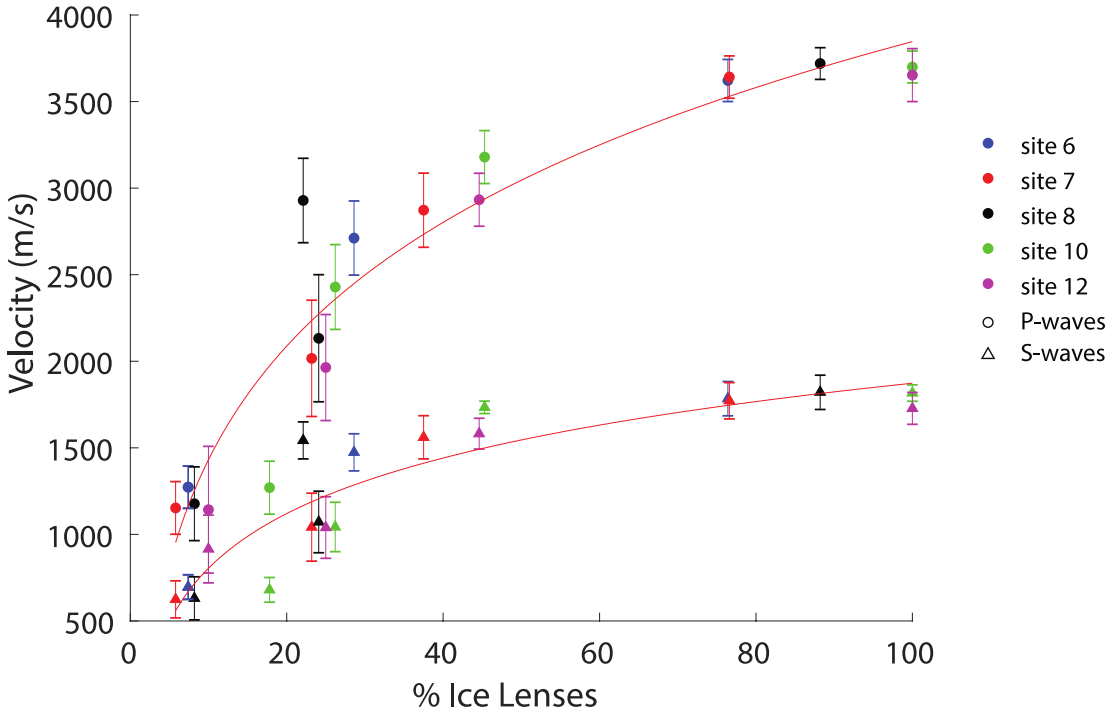

Figure 4.6: P-wave velocity vs Percentage of ice lenses. The P-waves from joint inversion 3 were used. The percentage of ice lenses were taken by measuring the total thickness of ice lenses present in each layer, divided by the thickness of the given layer, up to 30 m. The ice core data from Miller et al. (2017) was used.

Despite a general increase in seismic velocity with ice lens abundance, the seismic waves in our study are too long-wavelength to resolve thin ice lenses. As previously mentioned, the ice lenses themselves are on the orders of centimeters in thickness and the p-waves cannot detect anything smaller than ~15 m, or its resolution depth. Thus, it is more likely the bulk concentration of ice over a range of depths affects velocity. The ice stratigraphy observed in Miller et al (2017) is a result of the infiltration of surface melt water into the glacier, and the observable drainage from the percolation of the water front. Since the percolation is gravity driven, the extent of percolation is defined by a water front (*Pfeffer and Humphrey*, 1996). The depths, both shallow and deep, at which this water freezes exhibit clear ice that is interpreted as the depth where the pore spaces filled with water freeze, as shown by

the cores. Since the wavelength of the P-and S-waves are greater than 15 m and 7 m respectively, then they can more readily resolve the pore closure depth than any of the shallow structure, with the caveat of the aquifer later producing a shadow zone for S-waves. However, the surface waves are affected by the high attenuation of the firn and have wavelengths insensitive (>100 m) to the pore closure transition at 25-30 m depth.

4.3: Water content across Greenland

Seismology provides us a way of estimating water content stored within the firn aquifer. We find that the Montgomery et al. (2017) average storage capacity is 1634 ± 983 kg m^{-2}, the average storage capacity 1565 ± 769 kg m^{-2} using their method for calculating water content, and an average storage capacity of 1082 ± 443 kg m^{-2} using the updated water content calculated from Equation 11 using the S-wave velocities from the inversions. The primary differences between the Montgomery et al. (2017) and our data is the result of a thinner aquifer. For example, sites 10 and 11 in the previous study using solely P-waves underestimated the base of the aquifer, depths of 25.7 m and 23.8 m respectively. However, our study for these sites provide updated depths that agree with pore closures depths or firn-ice transitions, with depths of 29 m at both sites, which are in agreement given the uncertainties. The storage capacity using the updated method (Eq. 6) indicates the aquifer layer may have significantly less water than the previous calculation, but also is within uncertainties. As discussed in section 4.1, the shear wave inversions may not be reliable, thus we focus on the storage capacity calculated by Equation 6.

The areal extent of Greenland where firn aquifers across Greenland, detected by radar, is about 21,900 km^2 (*Miège et al*. 2016). However, the lower part of the percolation zone, where meltwater is stored, is believed to span an area of 150,000 km^2 (*Harper et al.* 2012; *Vandecrux et al.* 2019). Using the area of detected aquifer and the total area of the lower percolation zone, we can calculate the total mass of water that is likely retained across the ice sheet using the derived storage capacity and the area in which the aquifers are present. The mass of water from the storage capacity using the old method from Montgomery et al. (2017) and our inversions are 35.7×10^{12} kg and 34.1×10^{12} kg, which simplify to 35.7 ± 21.5 Gt and 34.1 ± 16.8 Gt of H_2O respectively. Across the entire ice sheet, the total mass of water that could reside in the percolation zone is ~235 ± 11 Gt of H_2O. Excluding the air bubbles in the aquifer, our inversions show the total amount of water is slightly less than the previous estimate. The detected aquifers alone account for ~15% of the total storage capacity within the firn throughout the Greenland ice sheet.

This can be extrapolated to the sea level rise stored within the aquifers, which is calculated from the mass of water required to raise the sea level by 1 mm. We use the following equations:

$$SA*\Delta h = Vol_{1mm\ SL\ rise} \tag{15}$$

where SA is the surface area of the earth (km^3), Δh is the addition to 1 mm of water to the sea level and $Vol_{1mm\ SL\ rise}$ is the volume of water required to raise the sea level by 1 mm in kg m^{-2}. The surface area of earth is 510×10^6 km^2, oceans cover roughly 71% of the total surface area of the earth (*Lutgens* 1992). From Equation 15, the volume of water needed to raise the sea level by 1 mm is about 360 km^3 or a mass of

360×10^{12} kg (360 Gt) of water. Thus, the total amount of water currently stored in the Helheim firn aquifers would raise the sea level by 0.06 ± 0.03 mm if they were to completely drain, which is 1-2% of the current rate of sea level change of 2.5-3.4 mm/yr (*Cazenave* et al. 2014). However, if we expand this number to potential aquifers across all of Greenland, the contribution of firn aquifers to the global sea level is 0.32-0.95 mm, ~13-40% of the annual rate of sea level rise.

The total discharge rate from the Greenland ice sheet is about 535 Gt/yr based on measurements taken between 2000 and 2012 (*Enderlin et al.* 2014). During 2000 and 2005, there was an 17% annual increase in discharge (*Enderlin et al. 2014*). The totality of the GIS is covered by 2.9×10^6 Gt of water content (*Bamber et al.* 2001). Assuming constant discharge rate with an annual increase in discharge of 17%, the entirety of Greenland ice would melt in ~55 years. If the percolation zone across Greenland were filled with firn aquifers, then the firn aquifers would account for ~44% of the annual discharge rate alone. Understanding the melting process and the amount of meltwater that is being held will help us prepare for the long-term effects from the melting of Greenland and determining the contribution of firn aquifers to meltwater is an essential component of mass balance on the Greenland ice sheet.

4.4: Future Work

Our study of S and P-waves, along with surface waves, revealed that even with homogenous and stratified firn, there exists considerable complexities in the wave propagation. The aquifer layer itself may produce a low-velocity zone for S-waves but not P-waves. Since we are using refracted waves, this creates a shadow

zone that would not be detected by S-waves turning within the layer. Also, this impedance contrast will trap S-wave energy in the near surface and form multiple reverberations in the shallow layers above the aquifer, creating a coda of energy following the P-waves that is observed in the data. With the reverberations influencing the travel time picks in the S-waves, a more precise method of picking these waves is needed. The following are a few ways that I suggest this study could be improved upon in future work.

- Improved synthetic modeling: a full model space to explore the distance and frequency a source would need to be to account for the effects of the presumed low velocity zone.
    - The rj-McMC relies on heterogeneity of the data set to create a representative probability distribution of the ensemble of model. A more refined model geometry would improve the resolution of the synthetic modeling, thus improve the quality of the inversion.
- Full Waveform inversion: this approach would use the waveform's entire content of seismic traces, where each unexplained residual data sample is assumed to come from some interaction within the medium, and a summation of over the sources and receivers locating anomalies (*Virieux et al.* 2017).
    - The full-waveform inversion can use the seismic waves used in our study, as well as the reverberations and any waves that follow, in an optimized inversion that can better image the subsurface.
- Bayesian inversion with more constraints: Killingbeck et al. (2018) developed a Bayesian inversion of seismic surface waves with depth constraints,

Multimodal Layered Transdimensional Inversion (MuLTI), that calculates the probability of shear waves as a function of depth from the Rayleigh wave dispersion as well as additional depth constraints such as GPR constrained layering (*Killingbeck et al.* 2018).

- Our inversion results are biased to the initial inputs such that the velocity jumps we see may be forced by the model, and the velocities derived are fit to match the initial model as much as possible, rather than creating a most likely model based off the data alone.
- Our surface wave data are Rayleigh wave data, so their algorithm is highly applicable to our problem. The depths to the aquifer from the GPR and density profiles as well as the depth to the pore closure depth from this study could all be implemented as depth constraints to improve the overall resolution of the aquifer.

4.5: Conclusions

In summary, the use of P-waves, S-waves, and surface waves in a joint inversion is a promising technique for improving the resolution of the Helheim firn aquifer across the upper 40 m. Here, we reproduced the results from Montgomery et al. (2017) and validated their results. Using their methods, we determine an overall decrease in the amount of water present in the aquifer to a storage capacity from 1634 ± 983 kg m^{-2} in Montgomery et al. (2017) to 1565 ± 769 kg m^{-2} in our study. The detected aquifer system along the coasts of Greenland is estimated to contain 34.1 ± 16.8 Gt of water, ~0.06 ± 0.03 mm. The storage capacity in the firn across Greenland

could contain ~235 ± 115 Gt of H_2O, a potential contribution of 13-20% of the mass loss from Greenland and a contribution of 0.32-0.95 mm of H_2O to the global sea level.

We incorporated new constraints, in shear waves, to refine the previous estimates. The joint inversion of P-waves, S-waves, and surface waves calculated the base of the aquifer to lie at a depth of 27.9 ± 3.5 m and the aquifer thickness averages to 10 ± 4 m, consistent with past studies. Similarly, we find that the pore closure depth calculated by the inversion corresponds to the seismic base of the aquifer. However, the shear waves derived structure has a high uncertainty that need additional study. Our results show that the surface waves can resolve firn above the aquifer but are sensitive to both attenuation and seismic velocity. We need independent constraints on attenuation and subsurface stratigraphy. We also detected the contamination of the S-wave picks by reverberations of P-waves caused by a low velocity zone. The rj-McMC inversion does not account for the LVZ, thus the results may be biased by the starting parameters rather than the true aquifer structure. We provide evidence of a low velocity zone in our synthetic forward modeling, where the LVZ is consistent with the presence of a water saturated layer. The future work detailed above will help improve the resolution of the dimensions of the aquifer, and a better quantify the water content within the firn aquifer system.

Appendices

Appendix A: Inversion Q_P and V_P/V_S ratio

In this Appendix, we present the V_P/V_S ratio and Q_P that were derived from the different inversions.

Figure A1: Joint Inversion 1: P-waves and surface wave dispersion

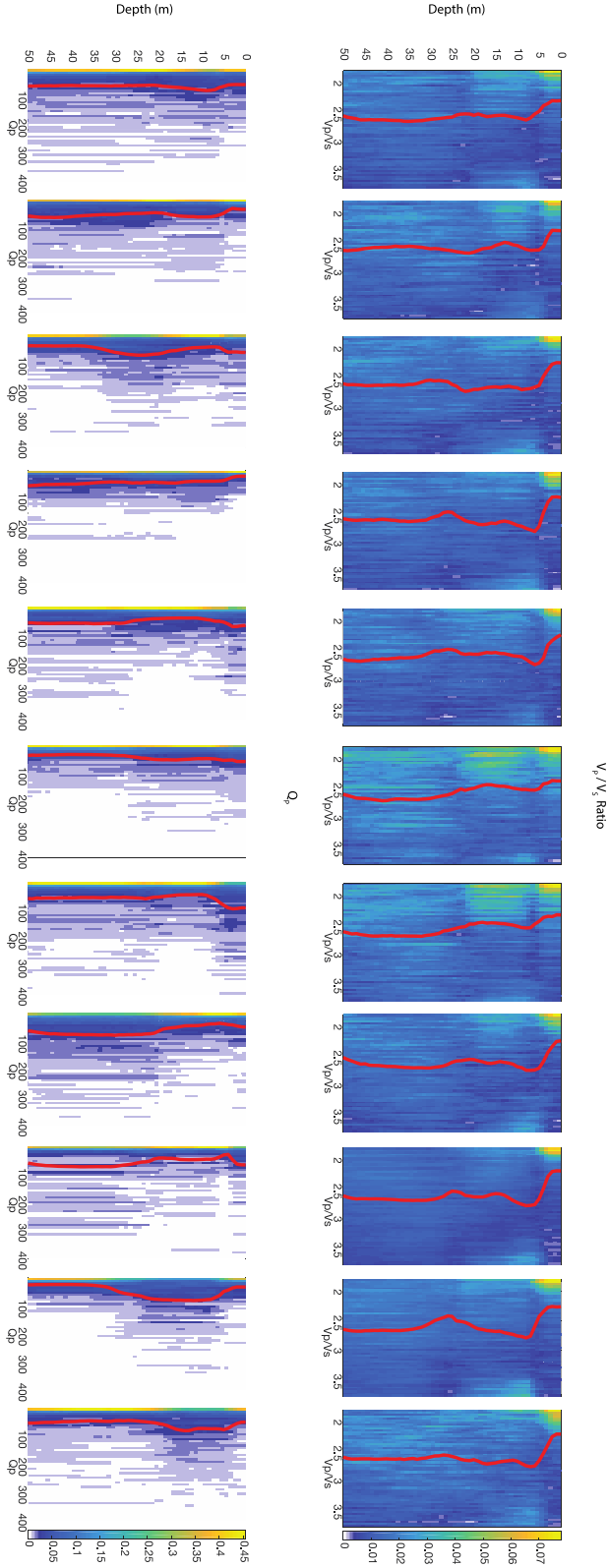

Figure A2: Joint inversion 2: P-wave and S-wave

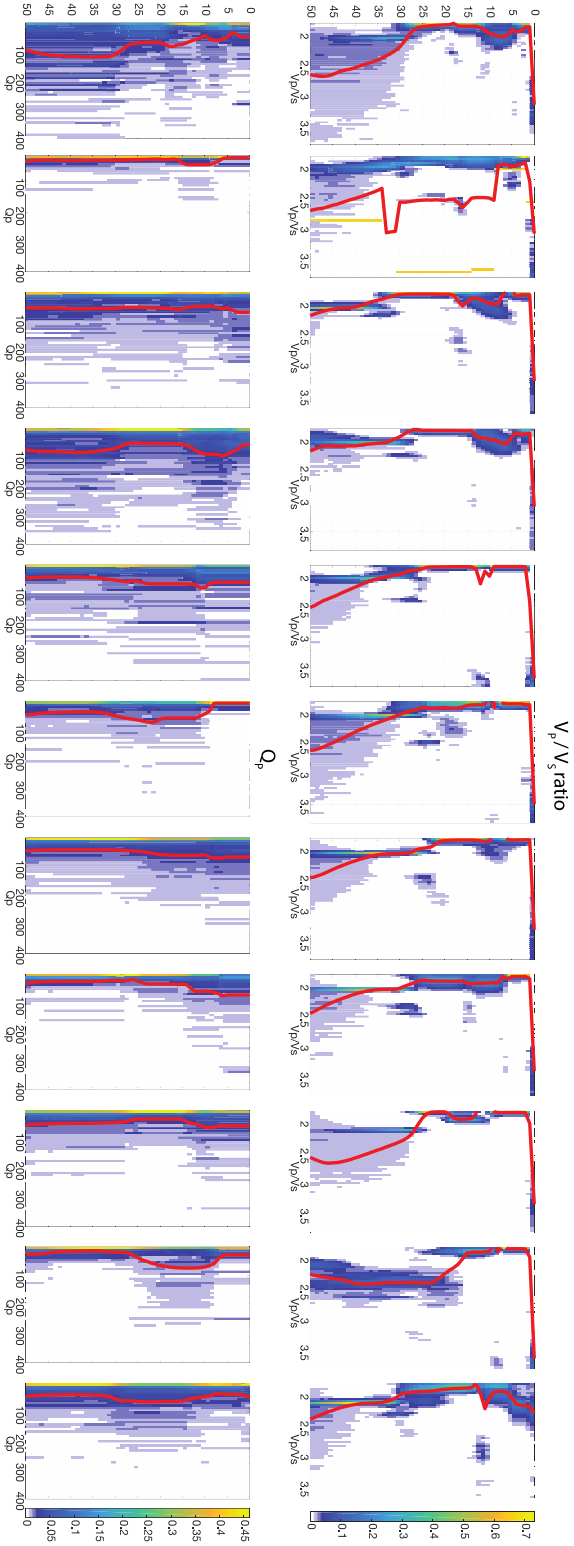

Figure A3: Joint inversion 3 – P-wave, S-wave and surface waves

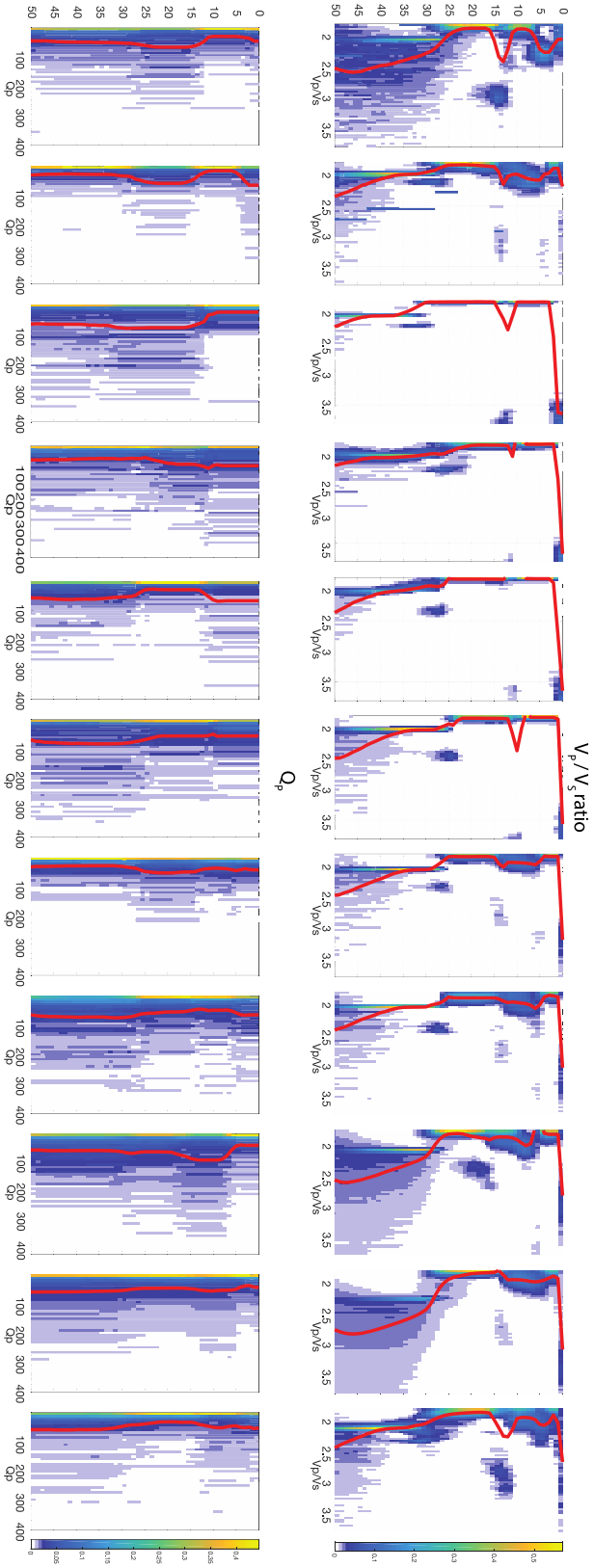

Appendix B: Inversion Misfit

In this Appendix, we present the misfit for every site for each inversion.

B1: Joint inversion 1

Figure B1.1: Site 1

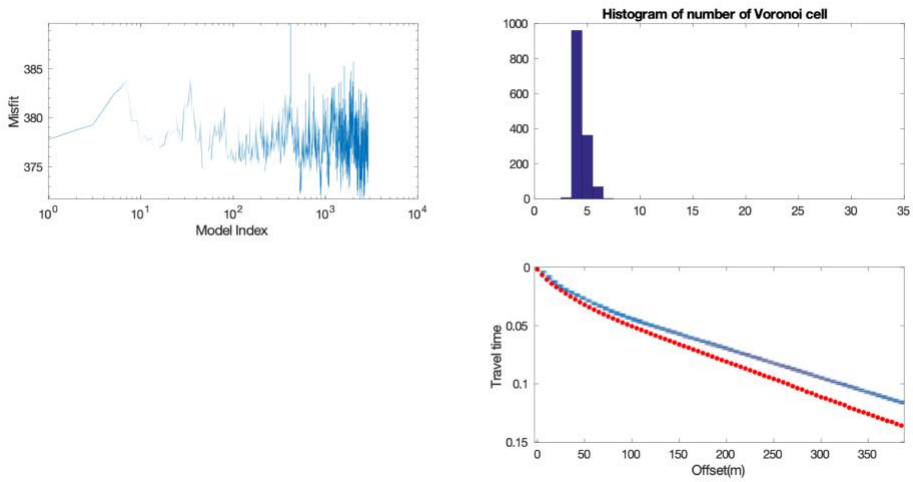

Figure B1.2: Site 2

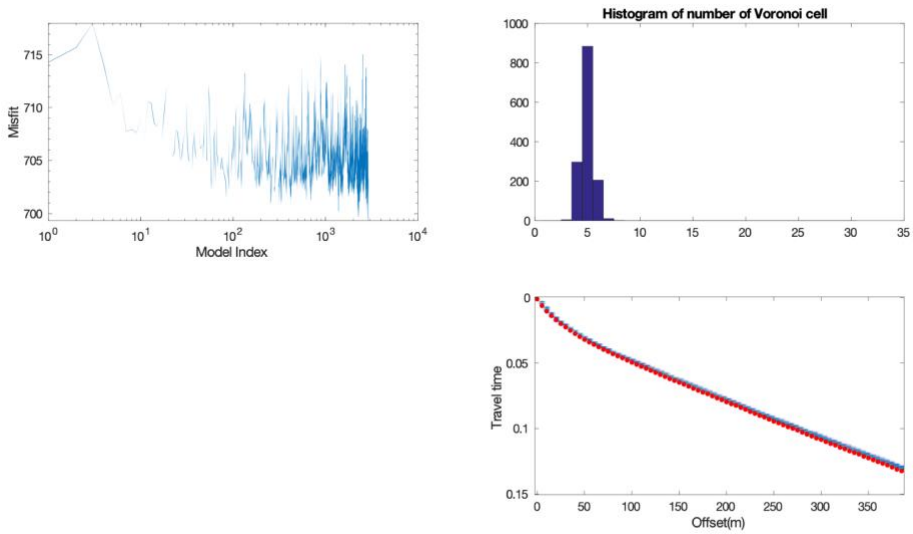

Figure B1.3: Site 3

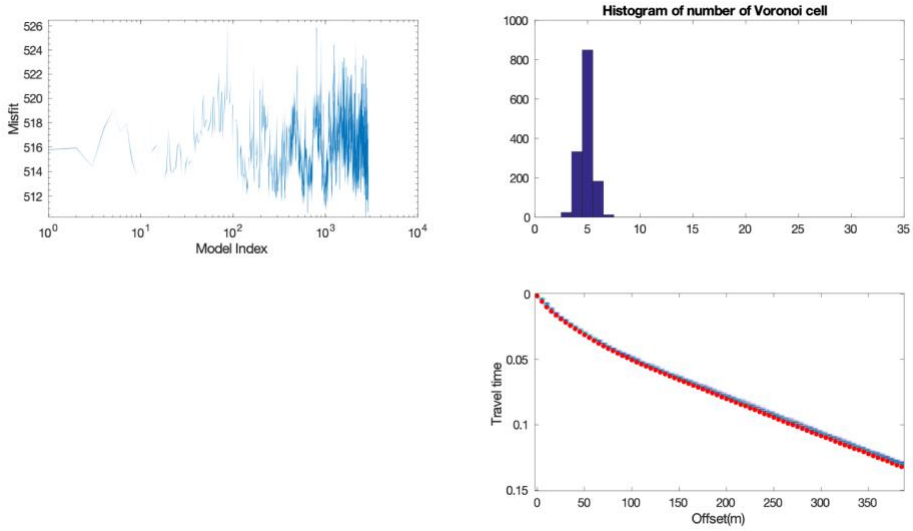

Figure B1.4: Site 4

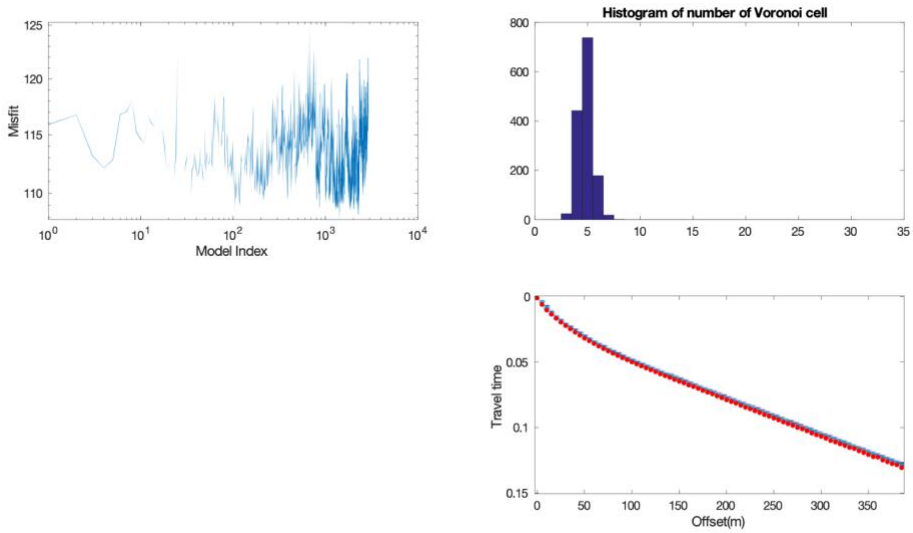

Figure B1.5: Site 5

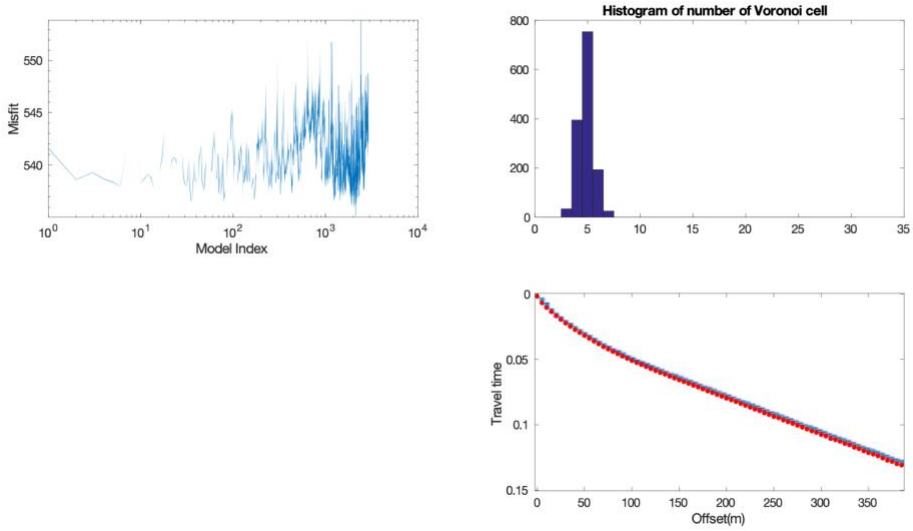

Figure B1.6: Site 6

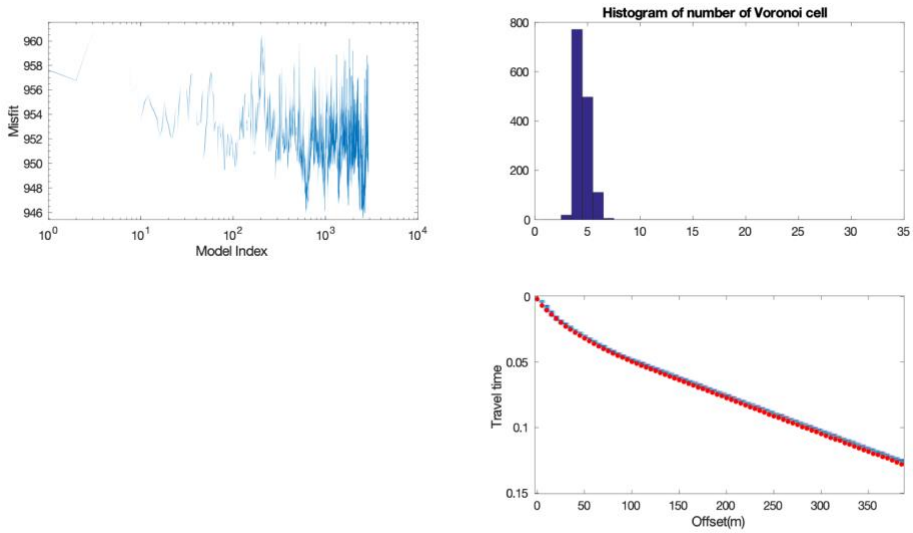

Figure B1.7: Site 7

Figure B1.8: Site 8

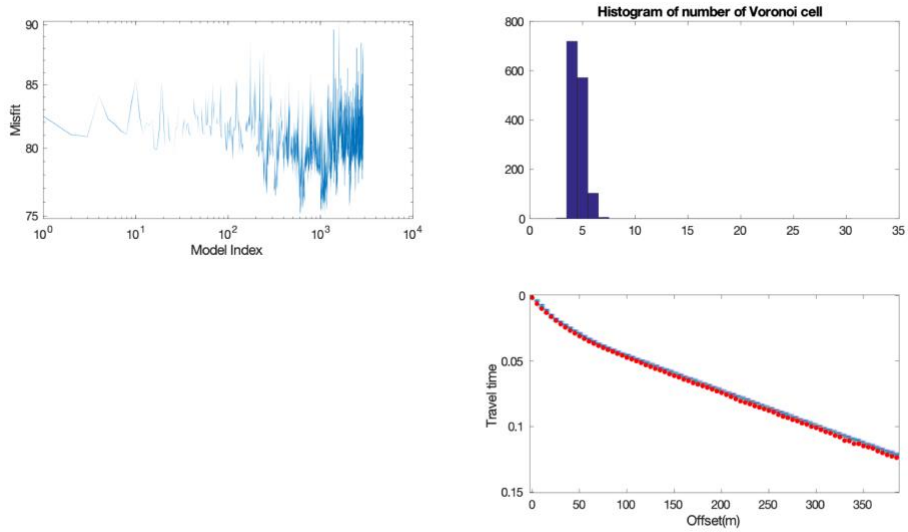

Figure B1.9: Site 10

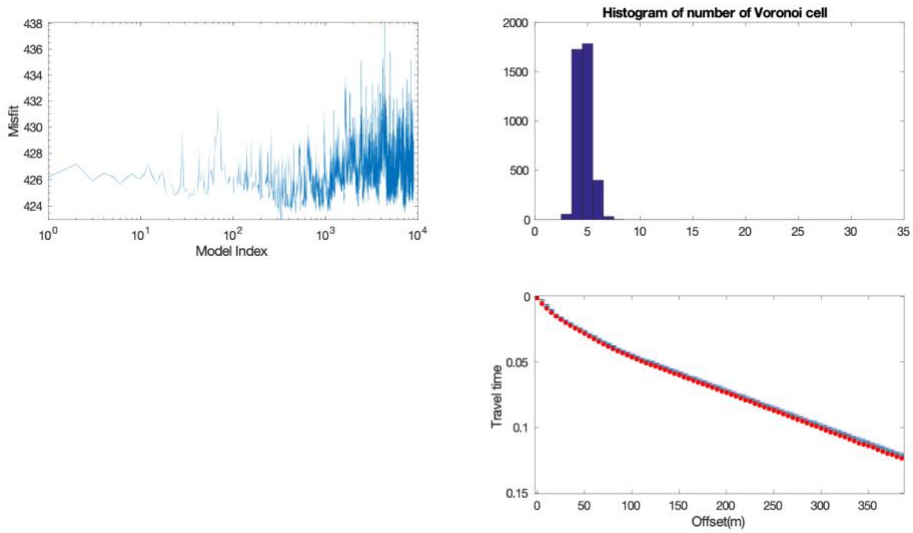

Figure B1.10: Site 11

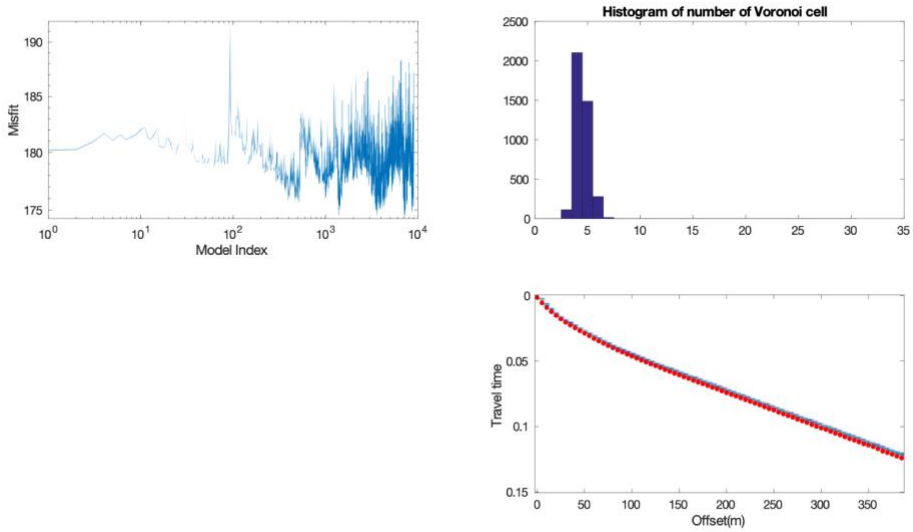

Figure B1.11: Site 12

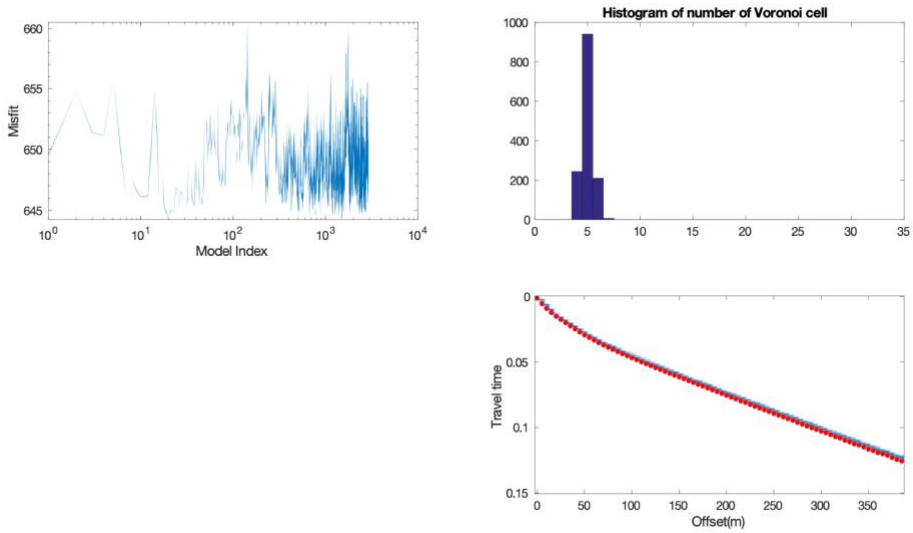

B2: Joint inversion 2

Figure B2.1: Site 1

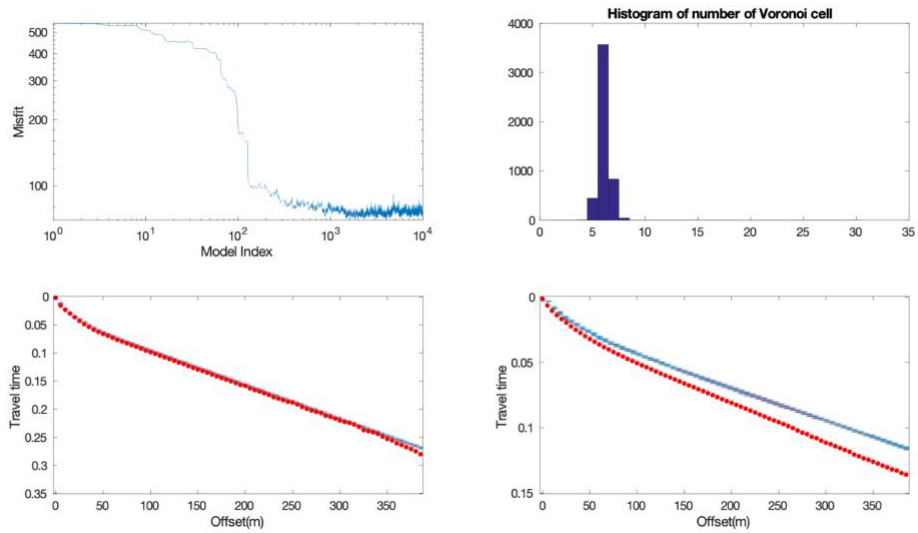

Figure B2.2: Site 2

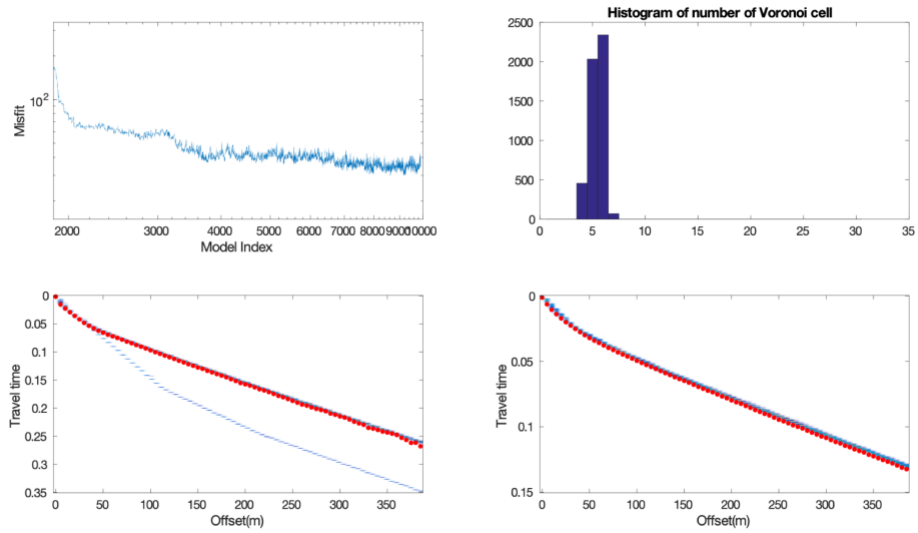

Figure B2.3: Site 3

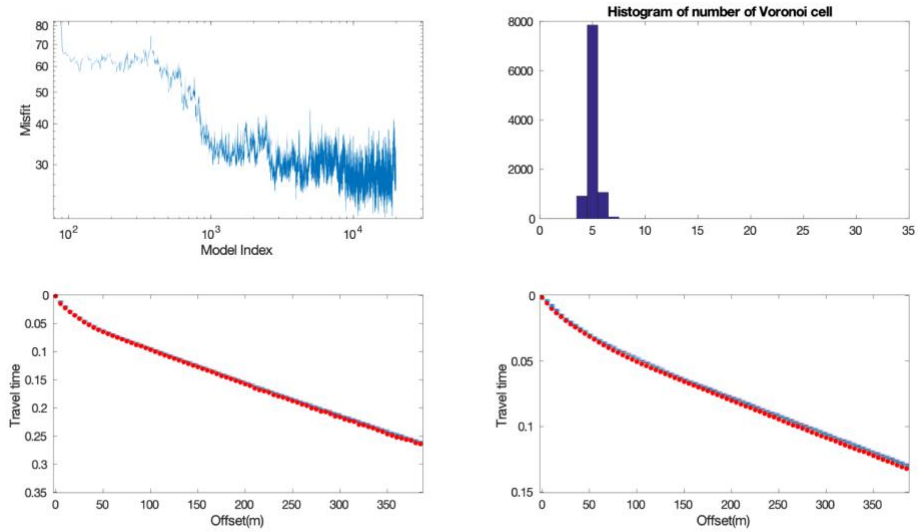

Figure B2.4: Site 4

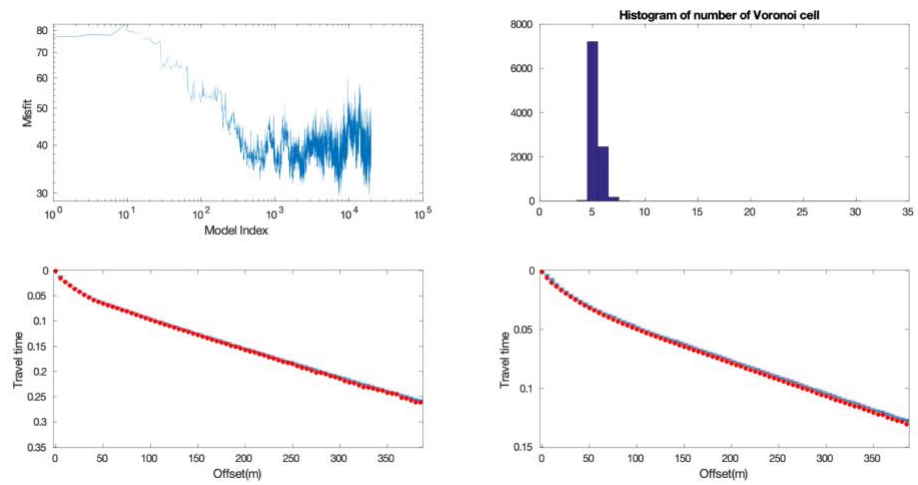

Figure B2.5: Site 5

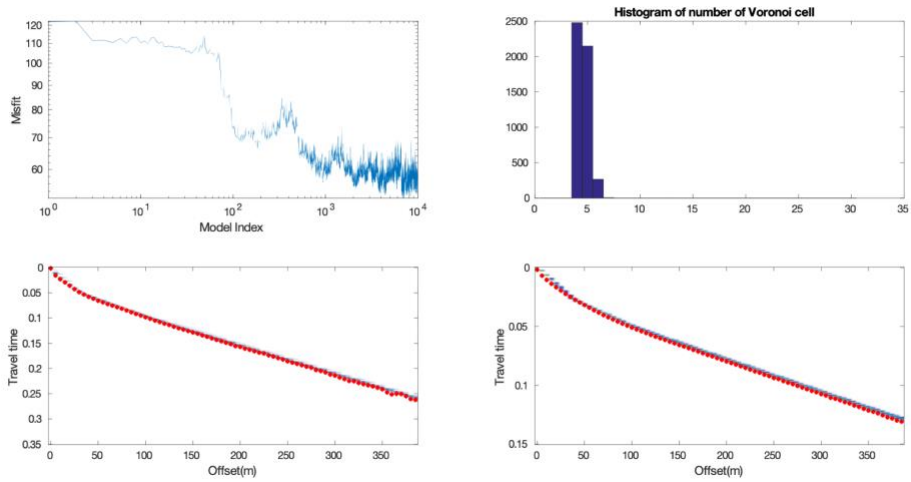

Figure B2.6: Site 6

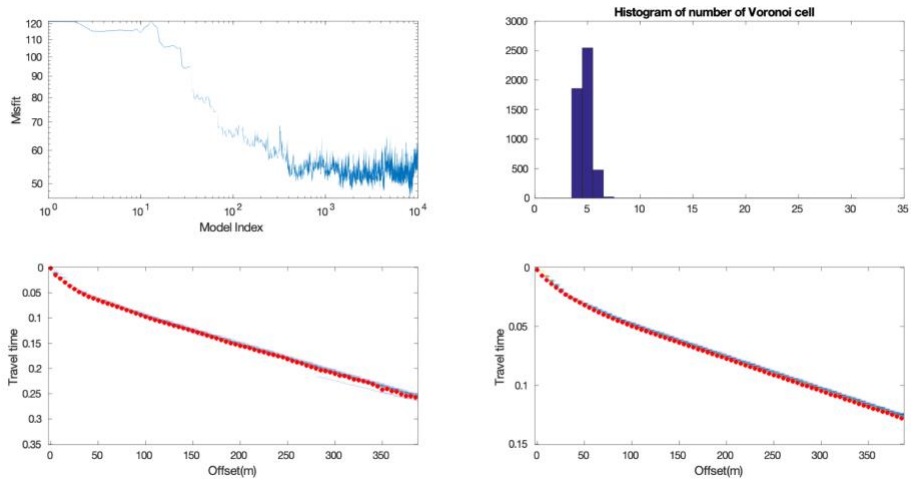

Figure B2.7: Site 7

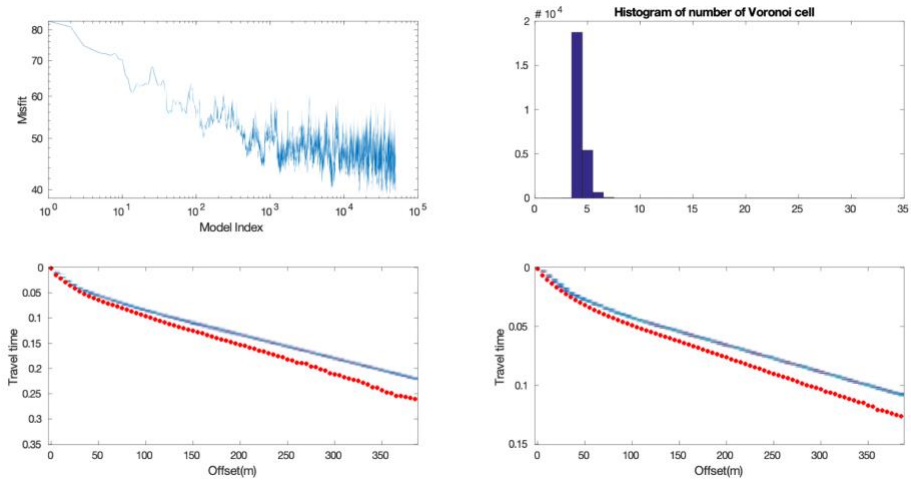

Figure B2.8: Site 8

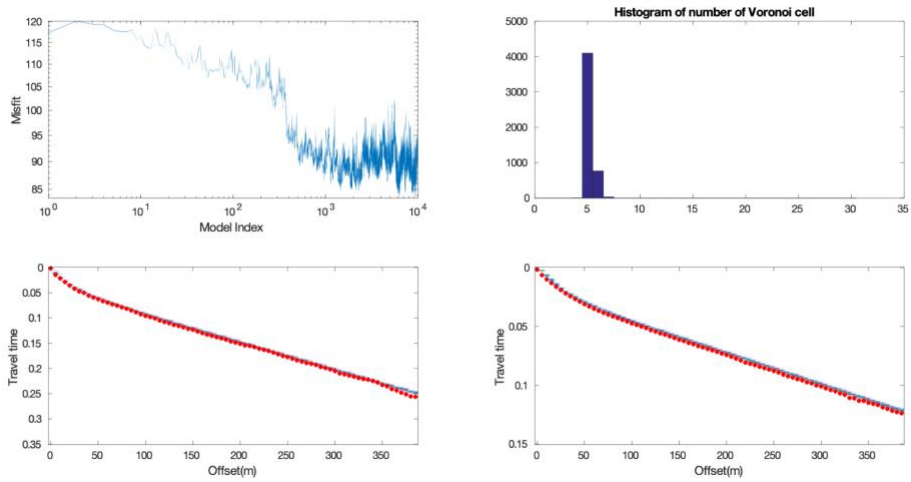

Figure B2.9: Site 10

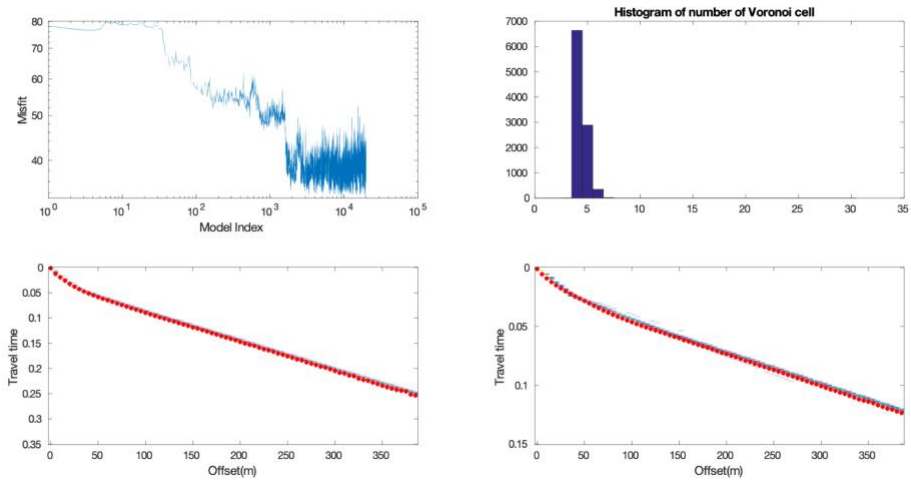

Figure B2.10: Site 11

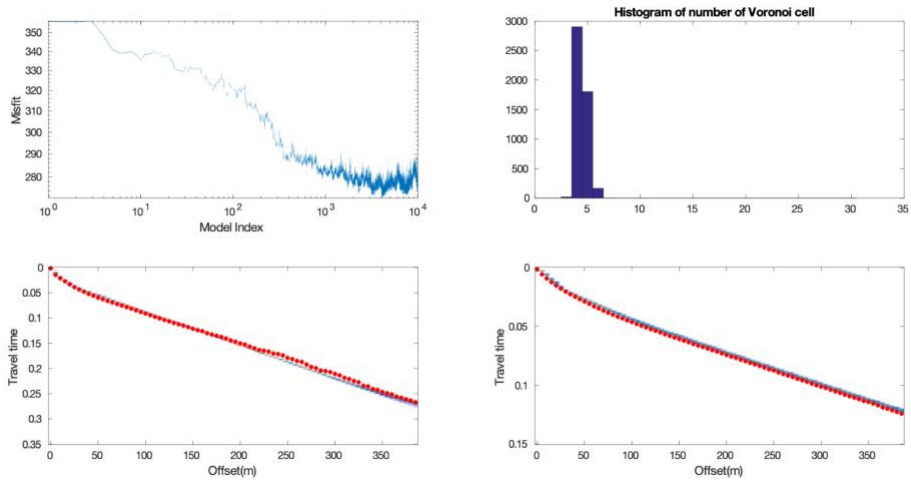

Figure B2.11: Site 12

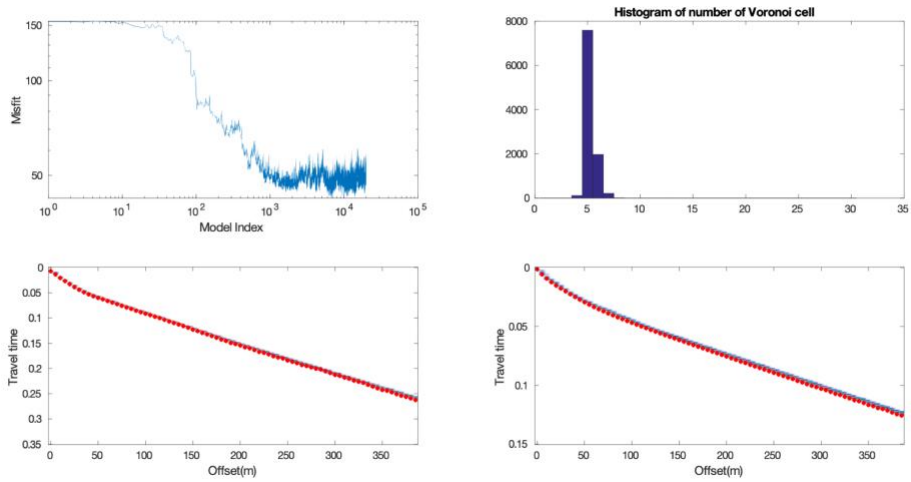

B3: Joint inversion 3

Figure B3.1: Site 1

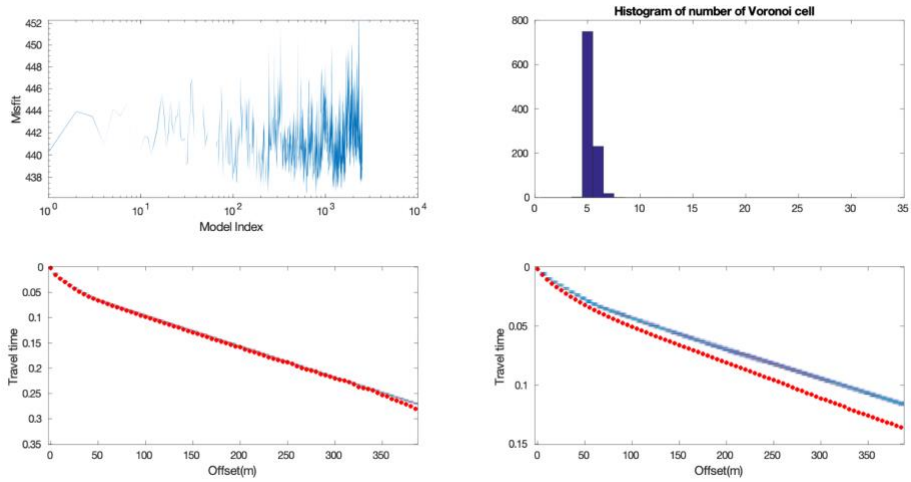

Figure B3.2: Site 2

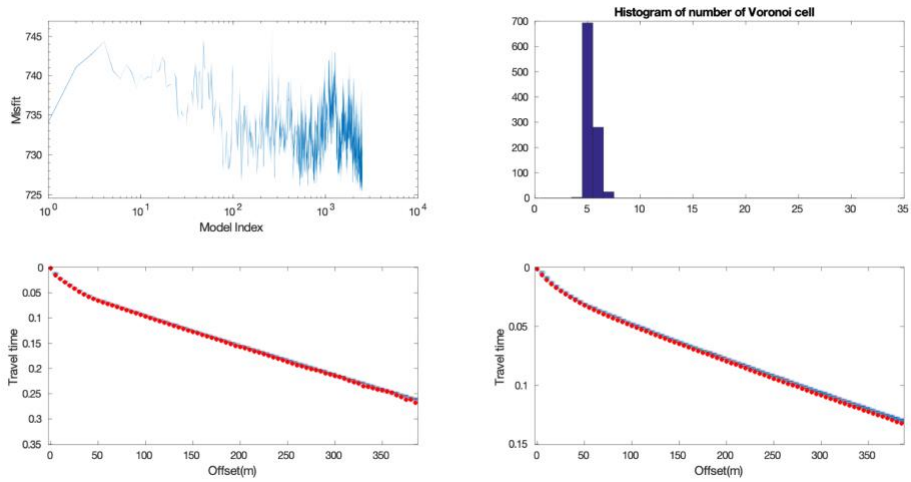

Figure B3.3: Site 3

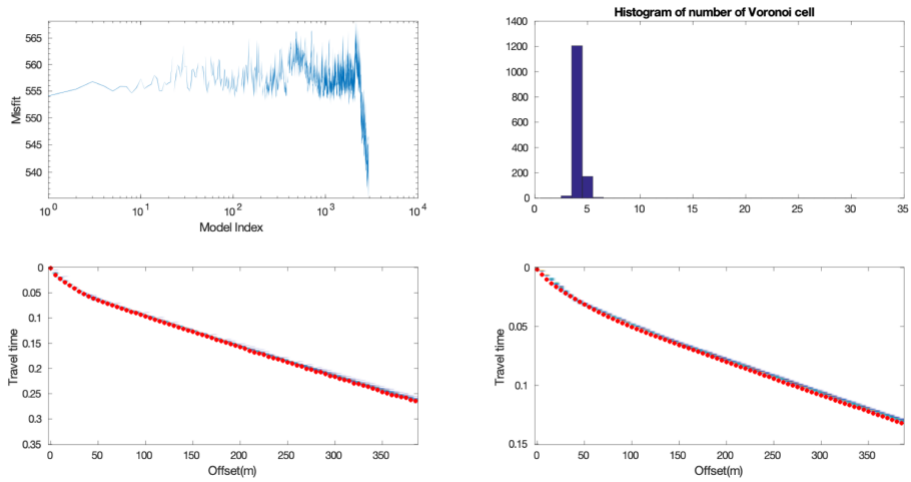

Figure B3.4: Site 4

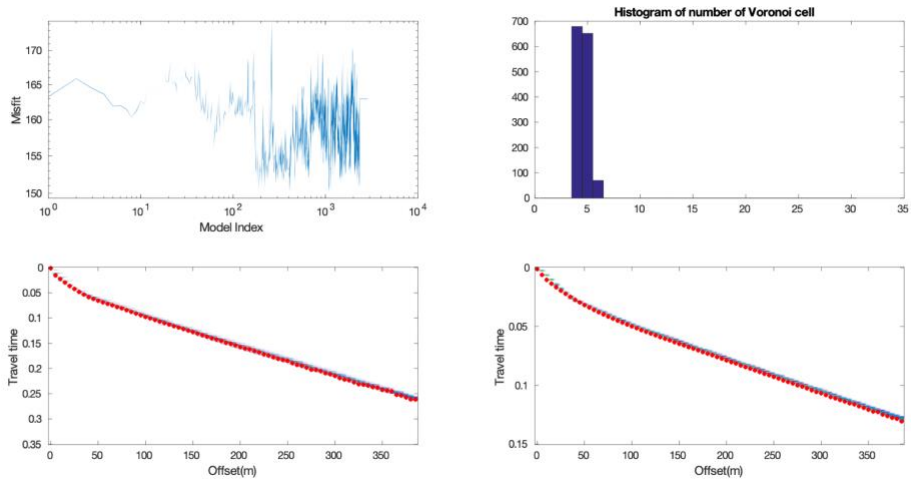

Figure B3.5: Site 5

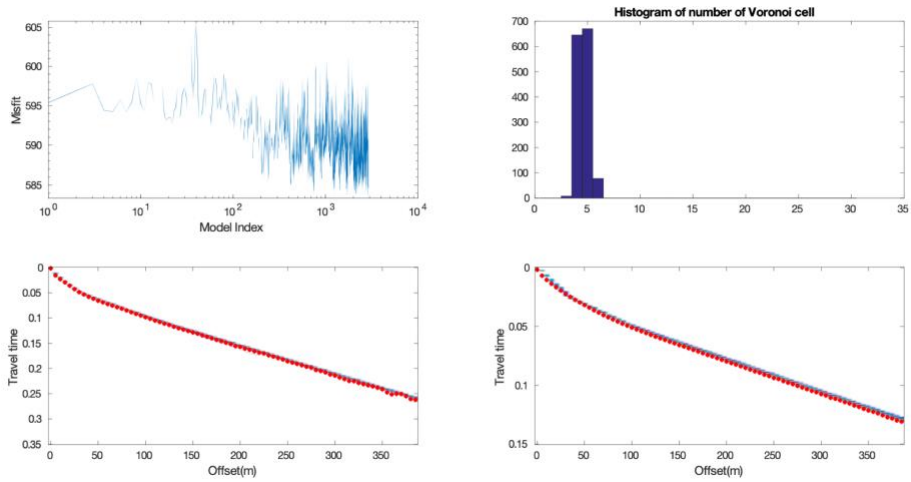

Figure B3.6: Site 6

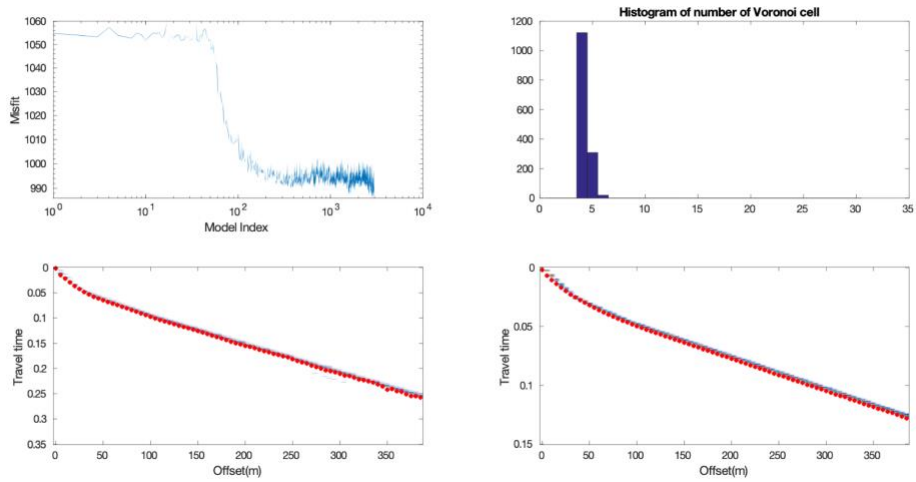

Figure B3.7: Site 7

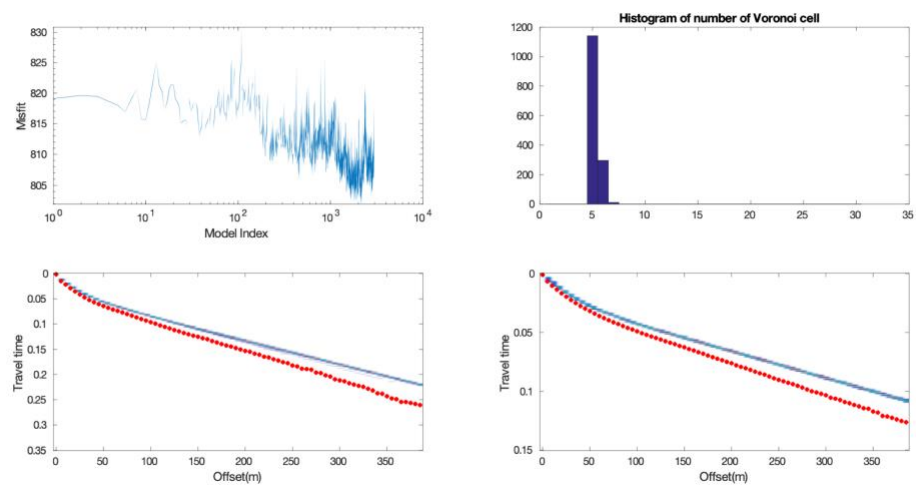

Figure B3.8: Site 8

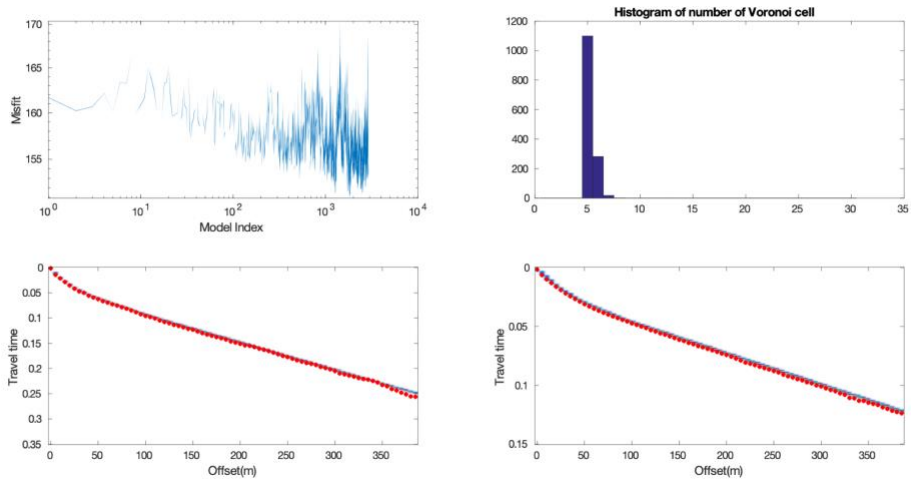

Figure B3.9: Site 10

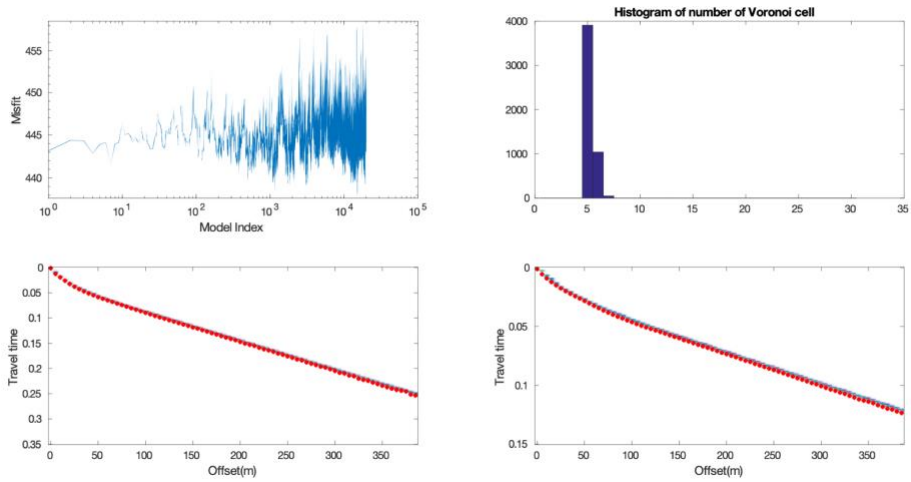

Figure B3.10: Site 11

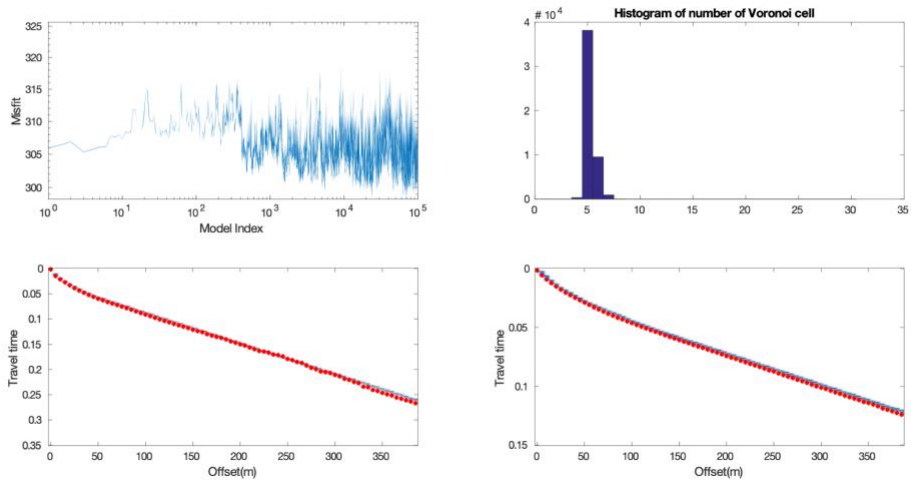

Figure B3.11: Site 12

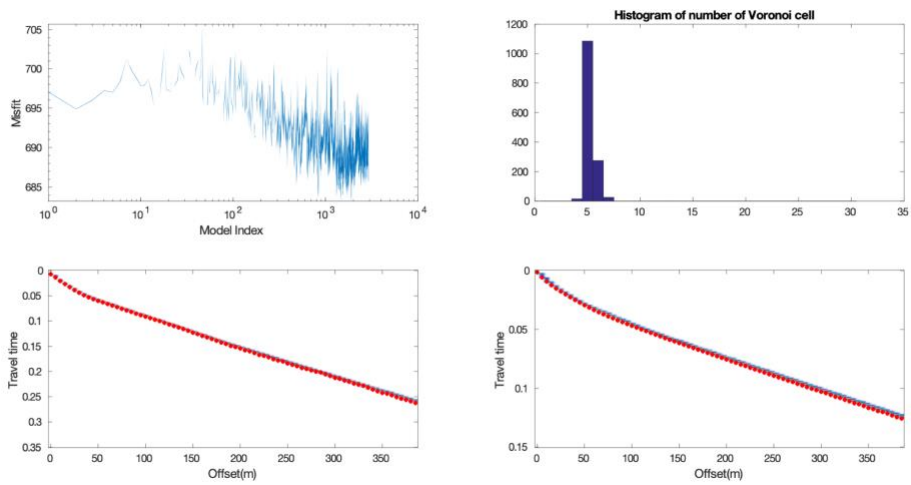

Bibliography

Aki, K., Richards, P. G., (1980). Quantitative Seismology: Theory and Methods. *W. H. Freeman & Co., New York*

Bamber, J. L., Layberry, R. L., & Gogineni, S. P. (2001a). A new ice thickness and bed data set for the Greenland ice sheet: 1. Measurement, data reduction, and errors. *Journal of Geophysical Research: Atmospheres*, *106*(D24), 33773–33780. https://doi.org/10.1029/2001JD900054

Bamber, J. L., Layberry, R. L., & Gogineni, S. P. (2001b). A new ice thickness and bed data set for the Greenland ice sheet: 1. Measurement, data reduction, and errors. *Journal of Geophysical Research: Atmospheres*, *106*(D24), 33773–33780. https://doi.org/10.1029/2001JD900054

Bamber, J. L., Tedstone, A. J., King, M. D., Howat, I. M., Enderlin, E. M., van den Broeke, M. R., & Noel, B. (2018). Land Ice Freshwater Budget of the Arctic and North Atlantic Oceans: 1. Data, Methods, and Results. *Journal of Geophysical Research: Oceans*, *123*(3), 1827–1837. https://doi.org/10.1002/2017JC013605

Biot, M. A. (1962). Mechanics of Deformation and Acoustic Propagation in Porous Media. *Journal of Applied Physics*, *33*(4), 1482–1498. https://doi.org/10.1063/1.1728759

Bodin, T., Sambridge, M., Tkalčić, H., Arroucau, P., Gallagher, K., & Rawlinson, N. (2012). Transdimensional inversion of receiver functions and surface wave dispersion: TRANSDIMENSIONAL INVERSION OF RF AND SWD. *Journal of Geophysical Research: Solid Earth*, *117*(B2), n/a-n/a. https://doi.org/10.1029/2011JB008560

Cazenave, A., Dieng, H.-B., Meyssignac, B., von Schuckmann, K., Decharme, B., & Berthier, E. (2014). The rate of sea-level rise. *Nature Climate Change*, *4*(5), 358–361. https://doi.org/10.1038/nclimate2159

Chandler, D. M., Wadham, J. L., Lis, G. P., Cowton, T., Sole, A., Bartholomew, I., et al. (2013). Evolution of the subglacial drainage system beneath the Greenland Ice Sheet revealed by tracers. *Nature Geoscience*, *6*(3), 195–198. https://doi.org/10.1038/ngeo1737

Christianson, K., Jacobel, R. W., Horgan, H. J., Anandakrishnan, S., & Alley, R. B. (2012). Subglacial Lake Whillans — Ice-penetrating radar and GPS observations of a shallow active reservoir beneath a West Antarctic ice stream. *Earth and Planetary Science Letters*, *331–332*, 237–245. https://doi.org/10.1016/j.epsl.2012.03.013

Christianson, K., Peters, L. E., Alley, R. B., Anandakrishnan, S., Jacobel, R. W., Riverman, K. L., et al. (2014). Dilatant till facilitates ice-stream flow in northeast Greenland. *Earth and Planetary Science Letters*, *401*, 57–69. https://doi.org/10.1016/j.epsl.2014.05.060

Chu, W., Schroeder, D. M., & Siegfried, M. R. (2018). Retrieval of Englacial Firn Aquifer Thickness From Ice-Penetrating Radar Sounding in Southeastern Greenland. *Geophysical Research Letters*, *45*(21), 11,770-11,778. https://doi.org/10.1029/2018GL079751

Clarke, T., & Echelmeyer, K. (1996). Seismic-reflection evidence for a deep subglacial trough beneath Jakobshavns Isbræ, West Greenland. *Journal of Glaciology*, *42*(141), 219-232. doi:10.3189/S0022143000004081

Drinkwater, M. R., Long, D. G., & Bingham, A. W. (2001). Greenland snow accumulation estimates from satellite radar scatterometer data. *Journal of Geophysical Research: Atmospheres*, *106*(D24), 33935–33950. https://doi.org/10.1029/2001JD900107

Enderlin, E. M., Howat, I. M., Jeong, S., Noh, M.-J., van Angelen, J. H., & van den Broeke, M. R. (2014). An improved mass budget for the Greenland ice sheet. *Geophysical Research Letters*, *41*(3), 866–872. https://doi.org/10.1002/2013GL059010

Flowers, G. E. (2018). Hydrology and the future of the Greenland Ice Sheet. *Nature Communications*, *9*(1). https://doi.org/10.1038/s41467-018-05002-0

Forster, R. R., Box, J. E., van den Broeke, M. R., Miège, C., Burgess, E. W., van Angelen, J. H., et al. (2014). Extensive liquid meltwater storage in firn within the Greenland ice sheet. *Nature Geoscience*, *7*(2), 95–98. https://doi.org/10.1038/ngeo2043

Fountain, A. G., & Walder, J. S. (1998). Water flow through temperate glaciers. *Reviews of Geophysics*, *36*(3), 299–328. https://doi.org/10.1029/97RG03579

Gao, C., & Lekić, V. (2018). Consequences of parameterization choices in surface wave inversion: Insights from transdimensional Bayesian methods. *Geophysical Journal International*. https://doi.org/10.1093/gji/ggy310

Godio, A., & Rege, R. B. (2015). The mechanical properties of snow and ice of an alpine glacier inferred by integrating seismic and GPR methods. *Journal of Applied Geophysics*, *115*, 92–99. https://doi.org/10.1016/j.jappgeo.2015.02.017

GreenISE.pdf. (n.d.).

Hakuba, M. Z., Folini, D., Wild, M., & Schär, C. (2012). Impact of Greenland's topographic height on precipitation and snow accumulation in idealized simulations: IMPACT OF GREENLAND'S TOPOGRAPHIC HEIGHT. *Journal of Geophysical Research: Atmospheres*, *117*(D9), n/a-n/a. https://doi.org/10.1029/2011JD017052

Hamada, G. M. (2004). Reservoir Fluids Identification Using Vp/Vs Ratio? *Oil & Gas Science and Technology*, *59*(6), 649–654. https://doi.org/10.2516/ogst:2004046

Harper, J., Humphrey, N., Pfeffer, W. T., Brown, J., & Fettweis, X. (2012). Greenland ice-sheet contribution to sea-level rise buffered by meltwater storage in firn. *Nature*, *491*(7423), 240–243. https://doi.org/10.1038/nature11566

Helgerud, M. B., Waite, W. F., Kirby, S. H., & Nur, A. (2003). Measured temperature and pressure dependence of compressional (V_p) and shear (V_s) wave speeds in compacted, polycrystalline ice Ih. *Canadian Journal of Physics*, *81*(1–2), 81–87. https://doi.org/10.1139/p03-008

Hoffman, M. J., Catania, G. A., Neumann, T. A., Andrews, L. C., & Rumrill, J. A. (2011). Links between acceleration, melting, and supraglacial lake drainage of the western Greenland Ice Sheet. *Journal of Geophysical Research*, *116*(F4). https://doi.org/10.1029/2010JF001934

Horgan, H. J., Anandakrishnan, S., Jacobel, R. W., Christianson, K., Alley, R. B., Heeszel, D. S., et al. (2012). Subglacial Lake Whillans — Seismic observations of a shallow active reservoir beneath a West Antarctic ice stream. *Earth and Planetary Science Letters*, *331–332*, 201–209. https://doi.org/10.1016/j.epsl.2012.02.023

Huss, M. (2013). Density assumptions for converting geodetic glacier volume change to mass change. *The Cryosphere*, *7*(3), 877–887. https://doi.org/10.5194/tc-7-877-2013

Johnson, J. B. (1982). On the Application of Blot's Theory to Acoustic Wave Propagation in Snow, *Cold Regions Science and Technology*, *6*(1), 49-60. https://doi.org/10.1016/0165-232X(82)90044-1

Jordan, T. M., Williams, C. N., Schroeder, D. M., Martos, Y. M., Cooper, M. A., Siegert, M. J., et al. (2018). A constraint upon the basal water distribution and thermal state of the Greenland Ice Sheet from radar bed echoes. *The Cryosphere*, *12*(9), 2831–2854. https://doi.org/10.5194/tc-12-2831-2018

Kawashima, K., Yamada, T., & Wakahama, G. (1993). Investigations of internal structure and transformational processes from firn to ice in a perennial snow patch. *Annals of Glaciology*, *18*, 117-122. doi:10.3189/S0260305500011368

Killingbeck, S. F., Livermore, P. W., Booth, A. D., & West, L. J. (2018). Multimodal Layered Transdimensional Inversion of Seismic Dispersion Curves With Depth Constraints. *Geochemistry, Geophysics, Geosystems*. https://doi.org/10.1029/2018GC008000

Kirchner, J., & Bentley, C. (1979). Seismic Short-Refraction Studies on the Ross Ice Shelf, Antarctica. *Journal of Glaciology*, *24*(90), 313-319. doi:10.3189/S0022143000014830

Lee, M. W. (2003), Velocity ratio and its application to predicting velocities. *U.S. Geol. Surv*. Bull. *2197*, 19 pp

Legchenko, A., Miège, C., Koenig, L. S., Forster, R. R., Miller, O., Solomon, D. K., et al. (2018). Estimating water volume stored in the south-eastern Greenland firn aquifer using magnetic-resonance soundings. *Journal of Applied Geophysics*, *150*, 11–20. https://doi.org/10.1016/j.jappgeo.2018.01.005

Lliboutry, L. (1996). Temperate ice permeability, stability of water veins and percolation of internal meltwater. *Journal of Glaciology*,*42*(141), 201-211. doi:10.3189/S0022143000004068

McGrath, D., Colgan, W., Steffen, K., Lauffenburger, P., & Balog, J. (2011). Assessing the summer water budget of a moulin basin in the Sermeq Avannarleq ablation region, Greenland ice sheet. *Journal of Glaciology*, *57*(205), 954–964. https://doi.org/10.3189/002214311798043735

Miège, C., Forster, R. R., Brucker, L., Koenig, L. S., Solomon, D. K., Paden, J. D., et al. (2016). Spatial extent and temporal variability of Greenland firn aquifers detected by ground and airborne radars: Greenland Firn Aquifers. *Journal of Geophysical Research: Earth Surface*, *121*(12), 2381–2398. https://doi.org/10.1002/2016JF003869

Miller, O., Solomon, D. K., Miège, C., Koenig, L., Forster, R., Schmerr, N., et al. (2017). Direct Evidence of Meltwater Flow Within a Firn Aquifer in Southeast Greenland: Meltwater Flow Within Firn Aquifer. *Geophysical Research Letters*, *45*(1), 207–215. https://doi.org/10.1002/2017GL075707

Montgomery, L. N., Schmerr, N., Burdick, S., Forster, R. R., Koenig, L., Legchenko, A., et al. (2017). Investigation of Firn Aquifer Structure in Southeastern Greenland Using Active Source Seismology. *Frontiers in Earth Science*, *5*. https://doi.org/10.3389/feart.2017.00010

Moorman, B. J., & Michel, F. A. (2000). Glacial hydrological system characterization using ground-penetrating radar. *Hydrological Processes*, *14*(15), 2645–2667. https://doi.org/10.1002/1099-1085(20001030)14:15<2645::AID-HYP84>3.0.CO;2-2

Munneke, P. K., M. Ligtenberg, S. R., van den Broeke, M. R., van Angelen, J. H., & Forster, R. R. (2014). Explaining the presence of perennial liquid water bodies in the firn of the Greenland Ice Sheet: KUIPERS MUNNEKE ET AL. *Geophysical Research Letters*, *41*(2), 476–483. https://doi.org/10.1002/2013GL058389

Palmer, S., Shepherd, A., Nienow, P., & Joughin, I. (2011). Seasonal speedup of the Greenland Ice Sheet linked to routing of surface water. *Earth and Planetary Science Letters*, *302*(3–4), 423–428. https://doi.org/10.1016/j.epsl.2010.12.037

Park, C. B., Miller, R. D., & Xia, J. (1998). Imaging dispersion curves of surface waves on multi-channel record. In *SEG Technical Program Expanded Abstracts 1998* (pp. 1377–1380). Society of Exploration Geophysicists. https://doi.org/10.1190/1.1820161

Peters, L. E., Anandakrishnan, S., Alley, R. B., & Voigt, D. E. (2012). Seismic attenuation in glacial ice: A proxy for englacial temperature: ENGLACIAL TEMPERATURE FROM SEISMIC *Q*. *Journal of Geophysical Research: Earth Surface*, *117*(F2), n/a-n/a. https://doi.org/10.1029/2011JF002201

Rignot, E. (2006). Changes in the Velocity Structure of the Greenland Ice Sheet. *Science*, *311*(5763), 986–990. https://doi.org/10.1126/science.1121381

Rignot, E., & Mouginot, J. (2012). Ice flow in Greenland for the International Polar Year 2008-2009: ICE FLOW GREENLAND 2009. *Geophysical Research Letters*, *39*(11), n/a-n/a. https://doi.org/10.1029/2012GL051634

Rignot, E., Velicogna, I., van den Broeke, M. R., Monaghan, A., & Lenaerts, J. T. M. (2011). Acceleration of the contribution of the Greenland and Antarctic ice sheets to sea level rise: ACCELERATION OF ICE SHEET LOSS. *Geophysical Research Letters*, *38*(5), n/a-n/a. https://doi.org/10.1029/2011GL046583

Rignot, Eric, Mouginot, J., Scheuchl, B., van den Broeke, M., van Wessem, M. J., & Morlighem, M. (2019). Four decades of Antarctic Ice Sheet mass balance from 1979–2017. *Proceedings of the National Academy of Sciences*, *116*(4), 1095–1103. https://doi.org/10.1073/pnas.1812883116

Robertson, J., & Bentley, C. (1975). Investigation of Polar Snow Using Seismic Velocity Gradients. *Journal of Glaciology*, *14*(70), 39-48. doi:10.3189/S002214300001337X

Ross, N., Sole, A. J., Livingstone, S. J., Igneczi, Á., & Morlighem, M. (2018). Near-margin ice thickness and subglacial water routing, Leverett Glacier, Greenland. *Arctic, Antarctic, and Alpine Research*, *50*(1), S100007. https://doi.org/10.1080/15230430.2017.1420949

Sambridge, M., Bodin, T., Gallagher, K., & Tkalcic, H. (2012). Transdimensional inference in the geosciences. *Philosophical Transactions of the Royal Society A: Mathematical, Physical and Engineering Sciences*, *371*(1984), 20110547–20110547. https://doi.org/10.1098/rsta.2011.0547

Schmerr, N., (2018), Greenland firn aquifer impacts on ice sheet hydrology, near Helheim Glacier, Greenland, 2015-2016. Arctic Data Center, https://arcticdata.io/catalog/view/doi:10.18739/A2RB6W22B.

Smith, E. C., Smith, A. M., White, R. S., Brisbourne, A. M., & Pritchard, H. D. (2015). Mapping the ice-bed interface characteristics of Rutford Ice Stream, West Antarctica, using microseismicity: Mapping ICE-Bed Interface, Rutford. *Journal of Geophysical Research: Earth Surface*, *120*(9), 1881–1894. https://doi.org/10.1002/2015JF003587

Sommerfeld, R. A. (1982). A review of snow acoustics. *Reviews of Geophysics*, *20*(1), 62. https://doi.org/10.1029/RG020i001p00062

Steger, C. R., Reijmer, C. H., van den Broeke, M. R., Wever, N., Forster, R. R., Koenig, L. S., et al. (2017). Firn Meltwater Retention on the Greenland Ice Sheet: A Model Comparison. *Frontiers in Earth Science*, *5*. https://doi.org/10.3389/feart.2017.00003

Vandecrux, B., MacFerrin, M., Machguth, H., Colgan, W. T., van As, D., Heilig, A., et al. (2019). Firn data compilation reveals widespread decrease of firn air content in western Greenland. *The Cryosphere*, *13*(3), 845–859. https://doi.org/10.5194/tc-13-845-2019

Vaňková, I., Voytenko, D., Nicholls, K. W., Xie, S., Parizek, B. R., & Holland, D. M. (2018a). Vertical Structure of Diurnal Englacial Hydrology Cycle at Helheim Glacier, East Greenland. *Geophysical Research Letters*. https://doi.org/10.1029/2018GL077869

Vaňková, I., Voytenko, D., Nicholls, K. W., Xie, S., Parizek, B. R., & Holland, D. M. (2018b). Vertical Structure of Diurnal Englacial Hydrology Cycle at Helheim Glacier, East Greenland. *Geophysical Research Letters*. https://doi.org/10.1029/2018GL077869

Lee 2003 Velocity ratio and its application to predicting velocities. (2003). https://doi.org/10.3133/b2197

Wyllie, M. R. J., Gregory, A. R., & Gardner, L. W. (1956). ELASTIC WAVE VELOCITIES IN HETEROGENEOUS AND POROUS MEDIA. *GEOPHYSICS*, *21*(1), 41–70. https://doi.org/10.1190/1.1438217

Xia, J., Miller, R. D., & Park, C. B. (1999). Estimation of near-surface shear-wave velocity by inversion of Rayleigh waves. *GEOPHYSICS*, *64*(3), 691–700. https://doi.org/10.1190/1.1444578

Zimmerman, R. W., & King, M. S. (1986). The effect of the extent of freezing on seismic velocities in unconsolidated permafrost. *GEOPHYSICS*, *51*(6), 1285–1290. https://doi.org/10.1190/1.1442181

Zwally, J. H., & Jun, L. (2002). Seasonal and interannual variations of firn densification and ice-sheet surface elevation at the Greenland summit. *Journal of Glaciology*, *48*(161), 199–207. https://doi.org/10.3189/172756502781831403